J. Fluid Mech. (2020), *vol*. 902, A31. © The Author(s), 2020.
Published by Cambridge University Press
doi:10.1017/jfm.2020.621

Law of the wall for a temporally evolving vertical natural convection boundary layer

Junhao Ke[1],†, **N. Williamson**[1], **S. W. Armfield**[1], **S. E. Norris**[2] and **A. Komiya**[3]

[1]School of Aerospace, Mechanical and Mechatronic Engineering, The University of Sydney, Sydney, New South Wales 2006, Australia

[2]Department of Mechanical Engineering, The University of Auckland, Auckland 1010, New Zealand

[3]Institute of Fluid Science, Tohoku University, Sendai 980-8577, Japan

(Received 20 December 2019; revised 27 April 2020; accepted 21 July 2020)

The present study concerns a temporally developing parallel natural convection boundary layer with Prandtl number $Pr = 0.71$ over an isothermally heated vertical plate. Three-dimensional direct numerical simulations (DNS) with different initial conditions were carried out to investigate the turbulent statistical profiles of mean velocity and temperature up to $Gr_\delta = 7.7 \times 10^7$, where Gr_δ is the Grashof number based on the boundary layer thickness δ. By virtue of DNS, we have identified a constant heat flux layer (George & Capp, *Intl J. Heat Mass Transfer*, vol. 22, issue 6, 1979, pp. 813–826; Hölling & Herwig, *J. Fluid Mech.*, vol. 541, 2005, pp. 383–397) and a constant forcing layer in the near-wall region. In the close vicinity of the wall ($y^+ < 5$) a laminar-like sublayer has developed, and the temperature profile follows the linear relation, consistent with the studies of spatially developing flows (Tsuji & Nagano, *Intl J. Heat Mass Transfer*, vol. 31, issue 8, 1988, pp. 1723–1734); whereas such a linear relation cannot be observed for the velocity profile due to the extra buoyancy. Similar to earlier studies (Ng *et al.*, *J. Fluid Mech.*, vol. 825, 2017, pp. 550–572) we show that this buoyancy effect would asymptotically become zero if the Gr_δ is sufficiently large. Further away from the wall ($y^+ > 50$), there is a log-law region for the mean temperature profile as reported by Tsuji & Nagano (1988). In this region, the turbulent length scale which characterises mixing scales linearly with the distance from the wall once Gr_δ is sufficiently large. By taking the varying buoyancy into consideration with the robust mixing length model, a modified log-law for the mean velocity profile for $y^+ > 50$ is proposed. The effect of the initialization is shown to persist until relatively high Gr_δ as a result of slow adjustment of the buoyancy (temperature) profile. Once these differences are accounted for, we find excellent agreement with our two DNS cases and with the spatially developing data of Tsuji & Nagano (1988). In the limit of higher Gr_δ the velocity profile is expected to become asymptotic to momentum-dominated behaviour as buoyancy becomes increasingly weak in comparison with shear in the near-wall region.

Key words: buoyant boundary layers, turbulent convection, turbulent boundary layers

† Email address for correspondence: junhao.ke@sydney.edu.au

1. Introduction

The validity of the universal law of the wall, which describes the mean velocity profile in turbulent wall-bounded flows, has been widely accepted among fluid mechanics researchers since its original derivation by the pioneering works of Von Kármán (1930) and Prandtl (1932). According to the law of the wall, the mean velocity follows a linear relation with the wall-normal distance in the close vicinity of the wall (known as the viscous sublayer), and a logarithmic relation with the wall-normal distance further away from the wall (known as the log-law region). Townsend (1951, 1961, 1976), considered the local equilibrium between energy supply and dissipation, and proposed the groundbreaking attached eddy hypothesis which describes the energy-containing motions for those asymptotically high Reynolds number wall-bounded flows. This hypothesis, together with the mixing length hypothesis proposed by Prandtl (1925), provide a detailed description and modelling of the wall turbulence behaviour in the logarithmic region for momentum-dominated flows which was later supported by numerous studies (see, for example, Perry & Chong 1982; Granville 1989; Hutchins & Marusic 2007; Klewicki 2010; Marusic *et al.* 2013). A recent detailed review on this topic can be found in Marusic & Monty (2019).

However, it is widely acknowledged that the vertical turbulent natural convection boundary layer (NCBL), although bounded by the wall, does not follow the aforementioned law of the wall since the driving mechanisms are fundamentally different: instead of the shear stress (or, pressure gradient), the NCBL flow is driven by the buoyancy force caused by the density difference. The presence of the buoyancy force (and thus the coupling of the temperature field and the velocity field) greatly complicates the investigation of vertical NCBL flows. Early attempts have been reported by George & Capp (1979), who theoretically investigated the turbulent NCBL. In their similarity analysis, a constant heat flux layer is successfully identified in the near-wall region; whereas the constant local shear stress layer that is commonly found in the momentum-dominated wall-bounded flows is absent due to the presence of the buoyancy. By asymptotically matching the mean profiles in the buoyant sublayer, they obtained a power-law solution for the mean profiles. Their work was later extended by Shiri & George (2008), who showed that the velocity power-law solution by George & Capp (1979) to be inconsistent with the momentum integral for the NCBL. Based on a similarity analysis in a differentially heated channel, Shiri & George (2008) suggested the mean velocity profile is logarithmic in the buoyant sublayer. Tsuji & Nagano (1988) experimentally investigated a spatially developing NCBL up to $Gr_\delta = 1.0 \times 10^7 (Re_\tau \approx 60)$ using hot wire measurements. Here, Gr_δ is the Grashof number based on the boundary layer thickness δ and Re_τ is the friction Reynolds number based on the maximum mean velocity location. This experimental study demonstrated the absence of the conventional law of the wall in the velocity profile, confirming the findings suggested by George & Capp (1979). However, based on their measurements, Tsuji & Nagano (1988) empirically showed the existence of a conductive sublayer, where the normalized temperature profile increases linearly with the wall-normal distance, and a log-law region, where the normalized temperature follows a logarithmic relation to the wall-normal distance. Versteegh & Nieuwstadt (1999) investigated the scaling behaviour of the NCBL in a differentially heated vertical channel using direct numerical simulation (DNS). Their scaling analysis supported the power-law near-wall mean temperature scaling proposed by George & Capp (1979) for the spatially developing vertical NCBL, whereas the mean velocity profile is obtained in terms of a defect law for the mean velocity gradient. Hölling & Herwig (2005) drew an analogy between the temperature field in the NCBL and the velocity field in the forced flows,

proposed scaling laws and wall functions in the near-wall region for a spatially developing vertical NCBL. In their analysis, the Reynolds shear stress is modelled by eddy viscosity and a constant turbulent Prandtl number is assumed. By asymptotically matching the temperature gradients in the overlap layer, Hölling & Herwig (2005) suggested both velocity and temperature profiles follow a log-law. Their proposed log-law showed reasonable agreement with the measurements of Tsuji & Nagano (1988). Ng, Chung & Ooi (2013) appraised and compared the above scaling laws proposed by George & Capp (1979), Shiri & George (2008), Versteegh & Nieuwstadt (1999) and Hölling & Herwig (2005) in a differentially heated vertical channel using DNS. Based on the DNS data, they suggested a power-law scaling for the mean temperature in the overlap region, consistent with the scaling arguments of George & Capp (1979), Shiri & George (2008) and Versteegh & Nieuwstadt (1999). Abedin, Tsuji & Hattori (2009) showed that their temporally developing DNS data closely matches the experimental measurements for the spatially developing NCBL and confirmed the observations of Tsuji & Nagano (1988).

More recently, Nakao, Hattori & Suto (2017) numerically investigated the spatially developing NCBL up to $Gr_\delta = 5.0 \times 10^6$ using large eddy simulation and identified a logarithmic region, similar to Tsuji & Nagano (1988), for the temperature profile. Ng *et al.* (2017) investigated the NCBL in a differentially heated vertical channel using DNS, and found that the mean temperature profile follows the same linear relation as given by Tsuji & Nagano (1988) in the close vicinity of the wall. Such agreement in the near-wall temperature profile between the two types of NCBL (spatially developing NCBL and NCBL in a differentially heated channel) indicates that the flow structures of NCBL may share the same physics in the close vicinity of the wall and a universal law describing the near-wall behaviour may be applicable to other types of vertical NCBL, for example, NCBL in cavities. Based on the DNS results, Ng *et al.* (2017) demonstrated that conditional averaging the near-wall region on high wall shear events revealed convergence of the velocity profile in the near-wall region towards a more typical log-law profile as Gr_δ increased. Consequently, the authors suggested that the turbulent boundary layer would have a (laminar) Prandtl–Blasius scaling in the near-wall region at low Re_τ (or Gr_δ), whereas a turbulent boundary layer (in the sense of Prandtl and von Kármán) would be obtained at very high Gr_δ. Similar ideas are well developed for Rayleigh–Bénard convection (see, e.g. Grossmann & Lohse 2000, 2001) where very high Gr_δ conditions are thought to be required to achieve a bulk-dominated thermal convection regime. A key difference in Rayleigh–Bénard flow is that the buoyancy vector is not aligned with a wall-parallel flow direction. Unfortunately, the state of art data for the vertical NCBL is lacking in the high Gr_δ regime for turbulent vertical NCBLs. To the authors' knowledge, due to both the high Gr_δ requirements to obtain this regime and the increased complexity of the velocity-buoyancy coupling in the momentum, the efforts in the near-wall scaling analysis have not yet demonstrated a universal velocity law of the wall for the vertical NCBL.

The present study concerns the turbulent mean velocity and temperature profiles of an incompressible temporally developing NCBL along a vertical isothermally heated plate. Upon proper modelling of the buoyancy force and the Reynolds stress, the buoyancy effect is taken into consideration to empirically derive the law of the wall for both mean velocity and temperature profiles. Again we note that the buoyancy force, acting as the driving force in the NCBL, is relatively weak so that a large Grashof number is needed to achieve a high Reynolds number flow. The temporal framework enables us to investigate the NCBL at a higher Grashof number (more turbulent) in a more computationally efficient way. By imposing periodic boundary conditions in the streamwise and spanwise directions, the domain size and the number of finite volume grids are greatly reduced, resulting in

a cheaper computational cost. Further validation and benefits of the temporal framework can be seen in Kozul, Chung & Monty (2016). The temporal framework is also adapted to a number of flows that are generally thought spatially developing, for example, Abedin, Tsuji & Hattori (2010) for a turbulent forced convection flow, Kozul *et al.* (2016) for an unsteady Rayleigh layer and Ke *et al.* (2019) for a linear stability study of the NCBL flow.

The paper is organized as follows. Firstly, the mathematical description of the problem and the numerical method are given in § 2. The flow visualization and the preliminaries are shown in § 3. In § 4 the time history of the wall characteristics of the DNS are shown. In § 5 the mean profiles of the velocity and temperature in the close vicinity of the wall are derived theoretically and the role that the buoyancy plays in this region is discussed. Based on the force balance, § 6 proposes a modified logarithmic law for the mean velocity profile by empirically modelling the buoyancy force in § 6.1 and the Reynolds stress in § 6.2. Finally, § 7 briefly summarizes the findings of the present study.

2. Numerical method

The governing equations for the boundary layer flow considered here are the three-dimensional Navier–Stokes and the conservation equations of mass and thermal energy. By employing the Boussinesq approximation, the incompressible form of the equations is obtained, which, in their dimensional form, reads

$$\frac{\partial u_i}{\partial x_i} = 0, \tag{2.1a}$$

$$\frac{\partial u_i}{\partial t} + \frac{\partial u_i u_j}{\partial x_j} = -\frac{1}{\rho}\frac{\partial p}{\partial x_i} + \nu\frac{\partial^2 u_i}{\partial {x_j}^2} + g\beta\theta\delta_{i1}, \tag{2.1b}$$

$$\frac{\partial \theta}{\partial t} + \frac{\partial u_j \theta}{\partial x_j} = \kappa\frac{\partial^2 \theta}{\partial {x_j}^2}, \tag{2.1c}$$

where ν is the kinematic viscosity, κ is the thermal diffusivity, ρ is the density of the fluid, g is the gravitational acceleration pointing to the negative x direction, β represents the thermal expansion coefficient and $\theta = T - T_\infty$ is the temperature difference between the local temperature T and the ambient temperature T_∞. The Prandtl number, defined as the ratio of the kinematic viscosity to the thermal diffusivity, is given by

$$Pr \equiv \nu/\kappa = 0.71, \tag{2.2}$$

for the problem under consideration. Here we follow the Einstein notation and the subscripts $i, j = 1, 2, 3$ denote the x, y, z axes which point in the streamwise, wall-normal and spanwise directions, respectively, so that $u_1,\ u_2,\ u_3 = u,\ v,\ w$. The temperature field (2.1*c*) is fully coupled to the velocity field through the buoyancy forcing term in the momentum equation (2.1*b*), where the Kronecker delta $\delta_{i1} = 1$ when $i = 1$ and $\delta_{i1} = 0$ otherwise.

The laminar analytical solution to the flow system (2.1) along an (doubly infinite) isothermal wall for $Pr \neq 1$, given by Illingworth (1950) and Schetz & Eichhorn (1962), can be expressed in the dimensional form

$$\bar{\theta}(\eta) = \theta_w \mathrm{erfc}(\eta), \tag{2.3a}$$

$$\bar{u}(\eta, t) = \frac{4g\beta\theta_w t}{1 - Pr}\left[\mathrm{i}^2\mathrm{erfc}(\eta) - \mathrm{i}^2\mathrm{erfc}\left(\frac{\eta}{\sqrt{Pr}}\right)\right], \tag{2.3b}$$

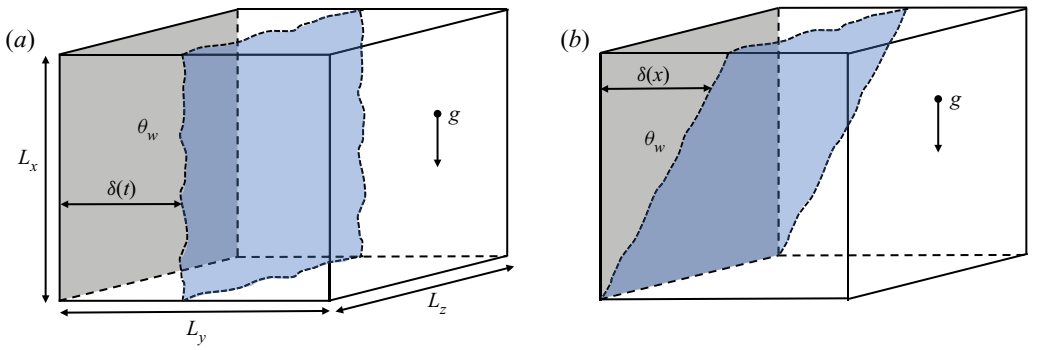

FIGURE 1. A systematic sketch (not to scale) of (*a*) the temporally evolving NCBL (present study), in contrast to (*b*) the canonical spatially developing NCBL in experiments (e.g. Tsuji & Nagano 1988).

where $\theta_w = T_w - T_\infty$ is the temperature difference between the isothermal wall and the ambient, $\eta = y/2\sqrt{\kappa t}$ is a similarity parameter, $\mathrm{erf}(\eta)$ is the error function of η, $\mathrm{erfc}(\eta) = 1 - \mathrm{erf}(\eta)$ is the complementary error function and $\mathrm{i}^n\mathrm{erfc}(\eta)$ is the nth integral of the complementary error function. The local (instantaneous) Grashof number Gr_δ and the boundary layer thickness δ are defined as

$$Gr_\delta \equiv \frac{g\beta\theta_w\delta^3}{\nu^2}, \quad \delta \equiv \int_0^\infty \frac{\bar{u}}{\bar{u}_m}\,\mathrm{d}y. \tag{2.4a,b}$$

Here, $\bar{(\cdot)}$ represents the mean (spatial average) quantities, obtained by taking the ensemble average in the homogeneous (x–z) plane (instead of in time, since the NCBL is unsteady) and $\bar{u}_m$ is the maximum mean streamwise velocity. It should be noted that from (2.3) the flow system depends upon η, the wall-normal coordinate scaled by diffusion time so that a streamwise and spanwise invariant parallel flow is obtained. Consequently, the boundary layer thickness and thus the Grashof number in (2.4) are essentially functions of time only, i.e. $\delta(t)$ and $Gr_\delta(t)$. A sketch of the computational domain is shown in figure 1(*a*). In the present study, we compare our temporally developing flow (see figure 1*a*) with a spatially developing NCBL (see figure 1*b*) by matching the boundary layer thickness δ (and therefore Gr_δ), as reported by Abedin *et al.* (2009). It is convenient to introduce the intrinsic length and velocity scales, given by

$$L_s = \kappa^{2/3}/(g\beta\theta_w)^{1/3}, \quad U_s = (\kappa g\beta\theta_w)^{1/3}, \tag{2.5a,b}$$

to describe the numerical set-up and results. Since the isothermal wall is unbounded in the homogeneous (x–z) plane and has no natural length scale, these intrinsic scales provide a flow regime independent normalization. In § 3 we revert to wall units for normalization of flow characteristics in the turbulent regime.

A uniform grid spacing is applied to the homogeneous directions (x and z) whilst the grid in the wall-normal direction is stretched with a maximum stretching rate of 3.56 %. Since the unsteady boundary layer is constantly evolving, the grid resolution in wall units Δ^+ is also changing with time. The detailed 'worst case' grid sizes are listed in table 1 when the smallest wall unit and smallest Kolmogorov scale η_k occur. To minimize the effect of the far-field boundary condition, the simulation is halted when the boundary layer thickness δ reaches 1/3 of the wall-normal domain size L_y. Such criteria are also used by Kozul *et al.* (2016) for a DNS study of a temporally evolving Rayleigh layer.

Case	Coordinate	Size L	Grids N	Mesh type	$\Delta^{\eta_k}_{min}$	$\Delta^{\eta_k}_{max}$	Δ^{+}_{min}	Δ^{+}_{max}	γ_{max}
DNS-A	x	$L_x = 1035L_s$	$N_x = 1024$	Uniform	2.56	2.56	4.36	4.36	—
	y	$L_y = 1035L_s$	$N_y = 512$	Stretched	0.47	6.26	0.81	10.8	3.56 %
	z	$L_z = 2070L_s$	$N_z = 2048$	Uniform	2.56	2.56	4.36	4.36	—
DNS-B	x	$L_x = 1035L_s$	$N_x = 1024$	Uniform	2.25	2.25	4.06	4.06	—
	y	$L_y = 1035L_s$	$N_y = 512$	Stretched	0.42	5.5	0.75	9.98	3.56 %
	z	$L_z = 1035L_s$	$N_z = 1024$	Uniform	2.25	2.25	4.06	4.06	—

TABLE 1. Grid sizes of the simulations. The grid size in Kolmogorov scale, Δ^{η_k}; the grid size in wall units, Δ^{+}, where the subscript *min* represents the smallest grid (first grid adjacent to the wall) and *max* represents the largest grid (far field); γ_{max} denotes the maximum stretching rate of the grid.

In order to initiate transition to turbulence, the analytical thermal field (2.3*a*) is augmented with temperature perturbations that decay towards the far field. In the present study, the streamwise temperature perturbation is given by

$$\theta'_x = \bar{\theta}(y) A_x \sum_{r=0}^{7} \sin\left(2^r \frac{2\pi x}{L_x}\right), \tag{2.6}$$

where $A_x = 10^{-3}$ is the amplitude and r is an integer specifying the components of the streamwise sinusoidal perturbation. For three-dimensional simulations, the superposition of a spanwise perturbation is necessary to trigger the three-dimensional transition mechanism (Nakao *et al.* 2017; Ke *et al.* 2019). To ensure the turbulent statistics for the temporally developing NCBL are indeed initial condition-invariant, two different spanwise (three-dimensional) perturbations are superposed on the flow

$$\theta'_z = \bar{\theta}(y) A_z \sin\left(\frac{2\pi n_z z}{L_z}\right), \quad \text{for DNS-A,} \tag{2.7a}$$

$$\theta'_0 = A_0[\mathrm{RAND}(0,1) - 0.5], \quad \text{for DNS-B,} \tag{2.7b}$$

respectively. Here, $A_z = 10^{-3}$ is the amplitude of the discrete spanwise mode and n_z is an integer specifying the spanwise perturbation mode for DNS-A; while RAND(0,1) denotes a random number generator which generates statistically uniformly distributed random numbers between 0 and 1 and $A_0 = 10^{-6}$ is the amplitude of the random (broadband) background noise for DNS-B. In the present study, $n_z = 23$ is chosen since it was observed empirically to be the most amplified spanwise mode in preliminary tests. The NCBL is initialized using the laminar analytical solution (2.3) at $Gr_\delta = 3000$. Details of the initial conditions are summarized in table 2.

While the perturbations are usually introduced to both the velocity and thermal fields spontaneously (broadband) for experiments (Cheesewright 1968; Tsuji & Nagano 1988) and large eddy simulation (Nakao *et al.* 2017), controlled perturbations (single field, discrete modes) are often used in DNS to investigate the transition–turbulent behaviour (Sayadi, Hamman & Moin 2013; Zhao, Lei & Patterson 2017). It should be noted that in the present study there is no velocity perturbation fed to the flow field as the velocity field will directly respond to the temperature perturbation through the buoyancy forcing term in (2.1*b*) while satisfying continuity (2.1*a*). A similar technique is used by a number of

Case	A_x	Spanwise perturbation	Initial temperature field	Initial Gr_δ
DNS-A	10^{-3}	(2.7*a*), with $A_z = 10^{-3}, n_z = 23$	$\theta(x, y, z) = \bar{\theta}(y) + \theta'_x + \theta'_z$	3000
DNS-B	10^{-3}	(2.7*b*), with $A_0 = 10^{-6}$	$\theta(x, y, z) = \bar{\theta}(y) + \theta'_x + \theta'_0$	3000

TABLE 2. Initial conditions for the simulation.

numerical NCBL studies (Janssen & Armfield 1996; Zhao, Lei & Patterson 2013; Zhao *et al.* 2017; Ke *et al.* 2019).

Periodic boundary conditions are imposed on the streamwise (x) and spanwise (z) boundaries to simulate the unbounded homogeneous plane. The velocity must vanish on the non-slip isothermal wall,

$$u = v = w = 0, \quad \theta = \theta_w, \quad \text{at } y = 0. \tag{2.8}$$

In the far field, the temperature decays to the quiescent condition with the flow remaining shear free,

$$\frac{\partial u}{\partial y} = \theta = v = w = 0, \quad \text{at } y = L_y. \tag{2.9}$$

With the boundary conditions (2.8) and (2.9), the flow system (2.1) is then numerically solved based on the settings in tables 1 and 2. For the details of the numerical method, readers are referred to Williamson, Armfield & Kirkpatrick (2012) and Ke *et al.* (2019).

3. Preliminaries

In the present study, we have employed two DNS (DNS-A and DNS-B) to ensure that the fully turbulent regime of the NCBL is independent of initialization. The different initializations of the spanwise perturbation, however, lead to different laminar–turbulent transition pathways for the NCBL, as demonstrated by figure 2. In DNS-A, the nonlinear interactions between the larger amplitude spanwise modes and the streamwise modes lead to an earlier three-dimensional transition, and the transition behaviour, shown in figure 2(*a–d*), is similar to that reported in spatially developing boundary layers (Fujii *et al.* 1970); whereas in DNS-B, the smaller initial background amplitude A_0 delays the transition so that the nonlinear interaction where energy is transferred between streamwise and spanwise modes occurs at a much higher Gr_δ (or time t) than in DNS-A. Here, δ_m is the distance from the wall at which the maximum mean streamwise velocity is located. In DNS-B, the accumulated momentum in the laminar regime undergoes transition via the ejection of the sprout-like convective rolls with the most unstable streamwise mode (Ke *et al.* 2019), as shown in figure 2(*e*,*f*). The detached convective rolls then begin to break into smaller scale structures, as depicted in figure 2(*g*), and finally attain the turbulent regime shown in figure 2(*h*). We conjecture that DNS-A represents a more 'natural transition' because of its similarity to previous experimental studies and that DNS-B as an example of a flow which undergoes a substantially different transition pathway. Nevertheless, despite the weakly three-dimensional transition for DNS-B, we will see later in § 6.4 that the velocity and temperature profiles proposed here are initial condition independent once the wall shear and wall heat flux are identified. The exact transition mechanism for DNS-B, however, is beyond the scope of the present study; we refer the interested readers to Ke *et al.* (2018, 2019).

Figure 3 illustrates the flow field visualization of the turbulent NCBL flow for DNS-A at $Gr_\delta = 7.7 \times 10^7$. Due to the presence of the wall, a boundary layer has developed in the near-wall region whereas the outer bulk flow shows a plume-like structure. The fine structures in figure 3(*a*) and the magnified view of the temperature and velocity contours in the near-wall region, given in figure 3(*b*,*c*), indicate that the flow is turbulent with a large range of scales of motion. Similar turbulent structure is also observed in DNS-B, as shown in figure 2(*h*).

By the end of simulation, DNS-A has reached $Gr_\delta = 7.7 \times 10^7$ ($Re_\tau = 147.99$); while DNS-B has achieved $Gr_\delta = 7.6 \times 10^7$ ($Re_\tau = 120.32$). Here, the friction Reynolds number is given by

$$Re_\tau = \frac{\delta_m u_\tau}{\nu}, \tag{3.1}$$

where u_τ is the friction velocity given by the wall shear stress τ_w,

$$u_\tau = \sqrt{\tau_w/\rho}, \quad \tau_w = \rho\nu \left.\frac{\partial \bar{u}}{\partial y}\right|_{y=0}. \tag{3.2a,b}$$

The viscous length scale, l_τ, is therefore given by

$$l_\tau = \frac{\nu}{u_\tau}. \tag{3.3}$$

The mean temperature and velocity profiles for the turbulent NCBL are fully described by the Reynolds averaged equations, where spatially averaging in homogeneous plane (x–z) is denoted by $\bar{(\cdot)}$. In wall units, the spatially averaged equations read

$$\frac{l_\tau}{{u_\tau}^2}\frac{\partial(u^+u_\tau)}{\partial(t^+l_\tau/u_\tau)} = \frac{\partial^2 u^+}{\partial {y^+}^2} - \frac{\partial(\overline{u'v'})^+}{\partial y^+} + Ri_w - Ri_\tau\theta^+, \tag{3.4a}$$

$$\frac{l_\tau}{u_\tau\theta_\tau}\frac{\partial(\theta^+\theta_\tau)}{\partial(t^+l_\tau/u_\tau)} = \frac{1}{Pr}\frac{\partial^2\theta^+}{\partial {y^+}^2} - \frac{\partial(\overline{v'\theta'})^+}{\partial y^+}, \tag{3.4b}$$

where

$$Ri_w \equiv \frac{g\beta l_\tau\theta_w}{{u_\tau}^2} = \frac{g\beta\nu\theta_w}{u_\tau^3}, \quad Ri_\tau \equiv \frac{g\beta l_\tau\theta_\tau}{{u_\tau}^2} = \frac{g\beta\nu q_w}{u_\tau^4}, \tag{3.5a,b}$$

are the friction Richardson number based on wall temperature difference and friction temperature, respectively, u^+ and θ^+ are the mean temperature and velocity in wall units, defined as

$$u^+ = \frac{\bar{u}}{u_\tau}, \quad \theta^+ = \frac{\theta_w - \bar{\theta}}{\theta_\tau}, \tag{3.6a,b}$$

and $(\overline{u'v'})^+$ and $(\overline{v'\theta'})^+$ are the Reynolds shear stress and the turbulent heat flux in wall units, given by

$$(\overline{u'v'})^+ = \frac{\overline{u'v'}}{{u_\tau}^2}, \quad (\overline{v'\theta'})^+ = -\frac{\overline{v'\theta'}}{u_\tau\theta_\tau}. \tag{3.7a,b}$$

The friction temperature θ_τ is given by the wall heat flux q_w and the friction velocity u_τ,

$$\theta_\tau = \frac{q_w}{\rho C_p u_\tau}, \quad q_w = -\rho C_p \kappa \left.\frac{\partial\bar{\theta}}{\partial y}\right|_{y=0}, \tag{3.8a,b}$$

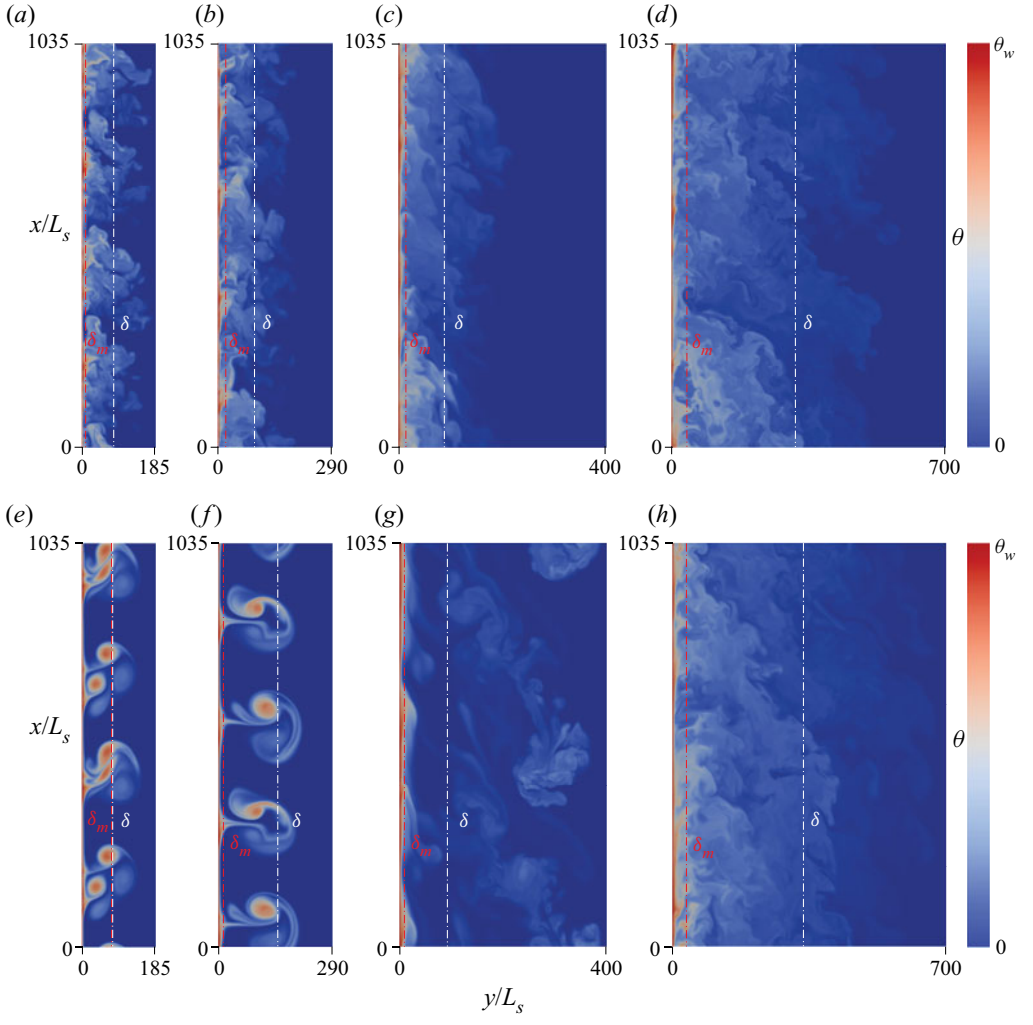

FIGURE 2. Visualization of the midspan temperature field for the laminar–turbulent transition of DNS-A (*a–d*) and DNS-B (*e–h*); (*a*) at $t = 154.32L_s/U_s$, $Gr_\delta = 1.1 \times 10^6$, with $\delta = 81.24L_s$ and $\delta_m = 8.78L_s$; (*b*) at $t = 168.04L_s/U_s$, $Gr_\delta = 1.6 \times 10^6$, with $\delta = 93.51L_s$ and $\delta_m = 18.79L_s$; (*c*) at $t = 245.19L_s/U_s$, $Gr_\delta = 3.2 \times 10^6$, with $\delta = 116.82L_s$ and $\delta_m = 13.62L_s$; (*d*) at $t = 558.97L_s/U_s$, $Gr_\delta = 6.4 \times 10^7$, with $\delta = 317.84L_s$ and $\delta_m = 29.98L_s$; (*e*) at $t = 154.32L_s/U_s$, $Gr_\delta = 8.9 \times 10^5$, with $\delta = 76.61L_s$ and $\delta_m = 76.46L_s$; (*f*) at $t = 168.04L_s/U_s$, $Gr_\delta = 7.1 \times 10^6$, with $\delta = 152.66L_s$ and $\delta_m = 11.32L_s$; (*g*) at $t = 245.19L_s/U_s$, $Gr_\delta = 3.6 \times 10^6$, with $\delta = 122.47L_s$ and $\delta_m = 10.44L_s$; (*h*) at $t = 558.97L_s/U_s$, $Gr_\delta = 7.6 \times 10^7$, with $\delta = 336.52L_s$ and $\delta_m = 29.96L_s$.

where C_p is the specific heat capacity of the fluid. Note the continuity equation (2.1*a*) vanishes as the derivatives in the homogeneous direction $\partial(\bar{\cdot})/\partial x$ and $\partial(\bar{\cdot})/\partial z$ and the mean wall-normal velocity $\bar{v}$ are all zero due to the parallel nature of the flow. From (3.4), a force balance and an energy balance can be obtained by integrating once with respect to

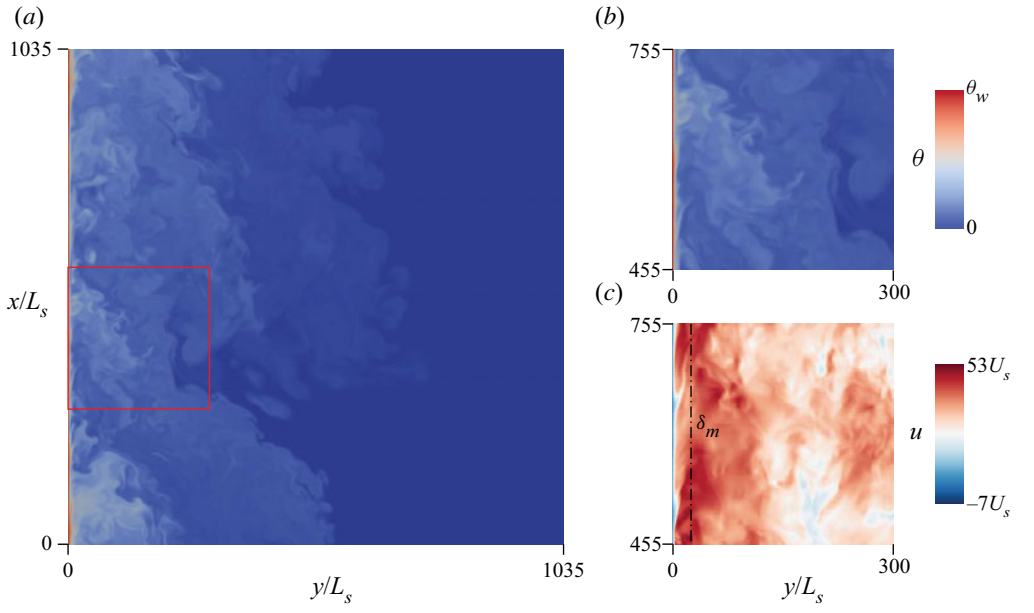

FIGURE 3. Visualization of the midspan flow field for DNS-A at $Gr_\delta = 7.7 \times 10^7$. (*a*) Temperature contours; (*b*) magnified temperature contours of the red box in panel (*a*); (*c*) magnified streamwise velocity contour of the red box in panel (*a*); dash-dotted line shows the maximum mean streamwise velocity location $\delta_m = 34.25L_s$.

the wall-normal distance y^+,

$$\int_0^{y^+} \frac{l_\tau}{{u_\tau}^2} \frac{\partial(u^+u_\tau)}{\partial(t^+l_\tau/u_\tau)}\,\mathrm{d}y^+ = \left.\frac{\partial u^+}{\partial y^+}\right|_0^{y^+} - (\overline{u'v'})^+|_0^{y^+} + \int_0^{y^+} (Ri_w - Ri_\tau\theta^+)\,\mathrm{d}y^+, \tag{3.9a}$$

$$\int_0^{y^+} \frac{l_\tau}{u_\tau\theta_\tau} \frac{\partial(\theta^+\theta_\tau)}{\partial(t^+l_\tau/u_\tau)}\,\mathrm{d}y^+ = \left.\frac{1}{Pr}\frac{\partial\theta^+}{\partial y^+}\right|_0^{y^+} - (\overline{v'\theta'})^+|_0^{y^+}. \tag{3.9b}$$

Given the boundary conditions at the wall, the integrated terms read

$$\left.\frac{\partial u^+}{\partial y^+}\right|_0^{y^+} = \frac{\partial u^+}{\partial y^+} - 1, \tag{3.10a}$$

$$(\overline{u'v'})^+|_0^{y^+} = (\overline{u'v'})^+, \tag{3.10b}$$

$$\left.\frac{1}{Pr}\frac{\partial\theta^+}{\partial y^+}\right|_0^{y^+} = \frac{1}{Pr}\frac{\partial\theta^+}{\partial y^+} - 1, \tag{3.10c}$$

$$(\overline{v'\theta'})^+|_0^{y^+} = (\overline{v'\theta'})^+, \tag{3.10d}$$

the balance equations (3.9) are therefore reduced to

$$\int_0^{y^+} \frac{l_\tau}{{u_\tau}^2} \frac{\partial (u^+ u_\tau)}{\partial (t^+ l_\tau / u_\tau)} \,\mathrm{d}y^+ = \frac{\partial u^+}{\partial y^+} - (\overline{u'v'})^+ + \int_0^{y^+} (Ri_w - Ri_\tau \theta^+) \,\mathrm{d}y^+ - 1, \tag{3.11a}$$

$$\int_0^{y^+} \frac{l_\tau}{u_\tau \theta_\tau} \frac{\partial (\theta^+ \theta_\tau)}{\partial (t^+ l_\tau / u_\tau)} \,\mathrm{d}y^+ = \frac{1}{Pr} \frac{\partial \theta^+}{\partial y^+} - (\overline{v'\theta'})^+ - 1. \tag{3.11b}$$

The individual contribution to the balance equations (3.11) are shown in figure 4. From figure 4(*a*), a constant heat flux region, where the molecular diffusion and turbulent heat flux balances the wall heat flux

$$q^+ \equiv \frac{1}{Pr} \frac{\partial \theta^+}{\partial y^+} - (\overline{v'\theta'})^+ \sim 1, \tag{3.12}$$

is found for $y^+ < 150$ at $Gr_\delta = 7.7 \times 10^7$. This is consistent with the existing literature (George & Capp 1979; Hölling & Herwig 2005; Wells & Worster 2008) where a constant heat flux layer is identified in the near-wall region for the turbulent spatially developing NCBL. Our results in figure 4(*b*) also show that an equilibrium is reached by the wall shear and the driving forces (buoyancy force and shear stress), where

$$F^+ \equiv \frac{\partial u^+}{\partial y^+} - (\overline{u'v'})^+ + \int_0^{y^+} (Ri_w - Ri_\tau \theta^+) \,\mathrm{d}y^+ \sim 1, \tag{3.13}$$

so that a constant forcing region (F^+ independent of y^+) is obtained. In the present study, we define the limit of the constant forcing region as the point where F^+ exceeds the wall shear stress τ_w^+ by 10 %, i.e. $F^+ = 1.1$. For $Gr_\delta = 7.7 \times 10^7$ (DNS-A), this gives a constant forcing region up to $y^+ = 150$ (which is approximately $y = \delta_m$). At lower Gr_δ, as indicated by figure 4(*c*), this constant forcing region extends to $y^+ = 60 (y = 0.6\delta_m)$ for $Gr_\delta = 2.1 \times 10^7$ (DNS-A); $y^+ = 70$ ($y = 0.6\delta_m$) for $Gr_\delta = 4.1 \times 10^7$ (DNS-A); and $y^+ = 100$ ($y = 0.8\delta_m$) for $Gr_\delta = 7.6 \times 10^7$ (DNS-B).

In the constant flux (and constant forcing) region, the right-hand sides of (3.11*a*) and (3.11*b*) both sum to zero, indicating the temporal evolution of the momentum and temperature (left-hand sides) are indeed negligible, and thus there exists a slowly varying near-wall region. With this in mind, the temporal evolution of the flow in the near-wall region can be ignored and for the purposes of developing mean profiles, a steady flow is assumed at each time instant.

4. Wall characteristics

Figure 5 depicts the development of the heat transfer of the NCBL in terms of Nusselt number Nu_δ and the wall shear stress (normalized by the boundary layer thickness δ) with Gr_δ (which grows with time t only). Here, the Nusselt number and the normalized wall shear are given by

$$Nu_\delta \equiv \frac{\delta q_w}{\rho C_p \kappa \theta_w}, \quad \tau_w^* = \tau_w / \rho g \beta \theta_w \delta. \tag{4.1a,b}$$

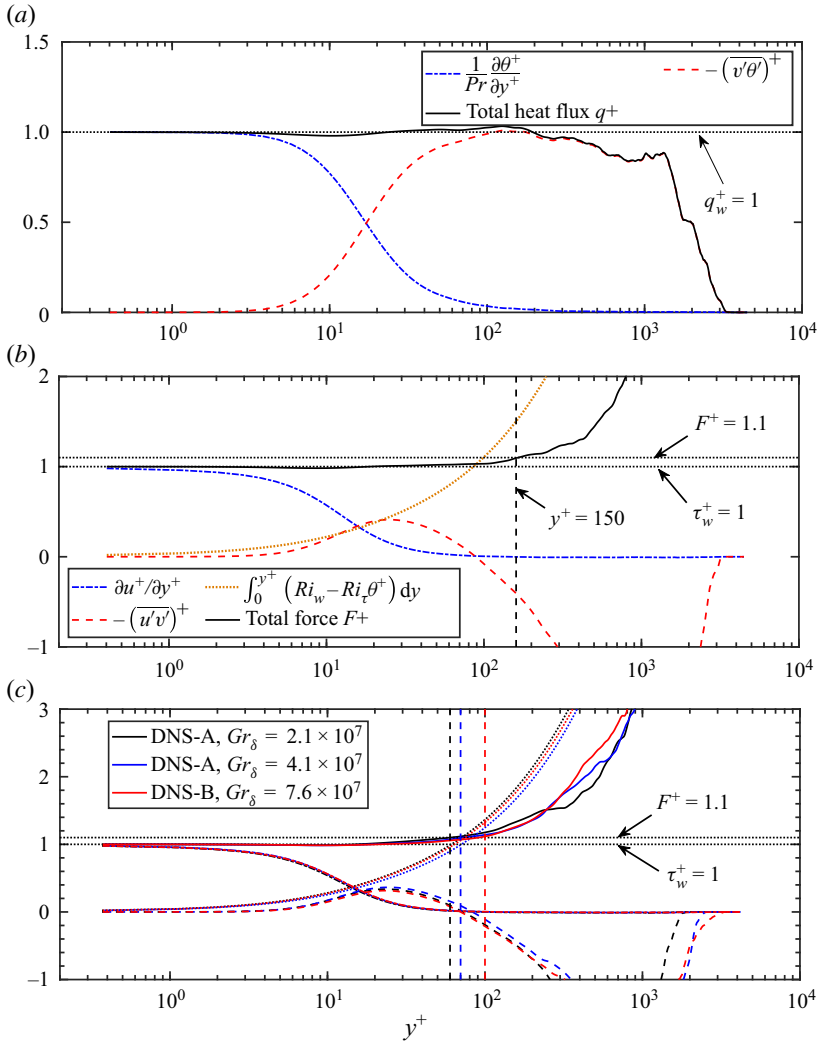

FIGURE 4. The near-wall statistics: (*a*) heat flux balance at $Gr_\delta = 7.7\times10^7$ (DNS-A); (*b*) force balance at $Gr_\delta = 7.7\times10^7$ (DNS-A); (*c*) force balances at $Gr_\delta = 2.1\times10^7$ (DNS-A), $Gr_\delta = 4.1\times10^7$ (DNS-A) and $Gr_\delta = 7.6\times10^7$ (DNS-B), with molecular shear $\partial u^+/\partial y^+$ (dash-dotted lines), Reynolds shear stress $-\overline{u'v'}$ (dashed lines), buoyancy force $\int_0^{y^+}(Ri_w - Ri_\tau\theta^+)\,\mathrm{d}y^+$ (dotted lines) and total force F^+ (solid lines); vertical dashed lines indicate the location when $F^+ = 1.1$ at corresponding Gr_δ.

At low Gr_δ, the Nusselt number and the normalized wall shear stress are Gr_δ independent, giving

$$Nu_\delta = \frac{1.71}{\sqrt{\pi}} = 0.965, \quad \tau_w^* = 0.302, \tag{4.2a,b}$$

according to the analytical solution (2.3) in the laminar conductive regime (e.g. Ke *et al.* 2019). At approximately $Gr_\delta = 10^6$, the spatially developing flows (Cheesewright 1968; Tsuji & Nagano 1988; Nakao *et al.* 2017) undergo transition to turbulence. In this regime,

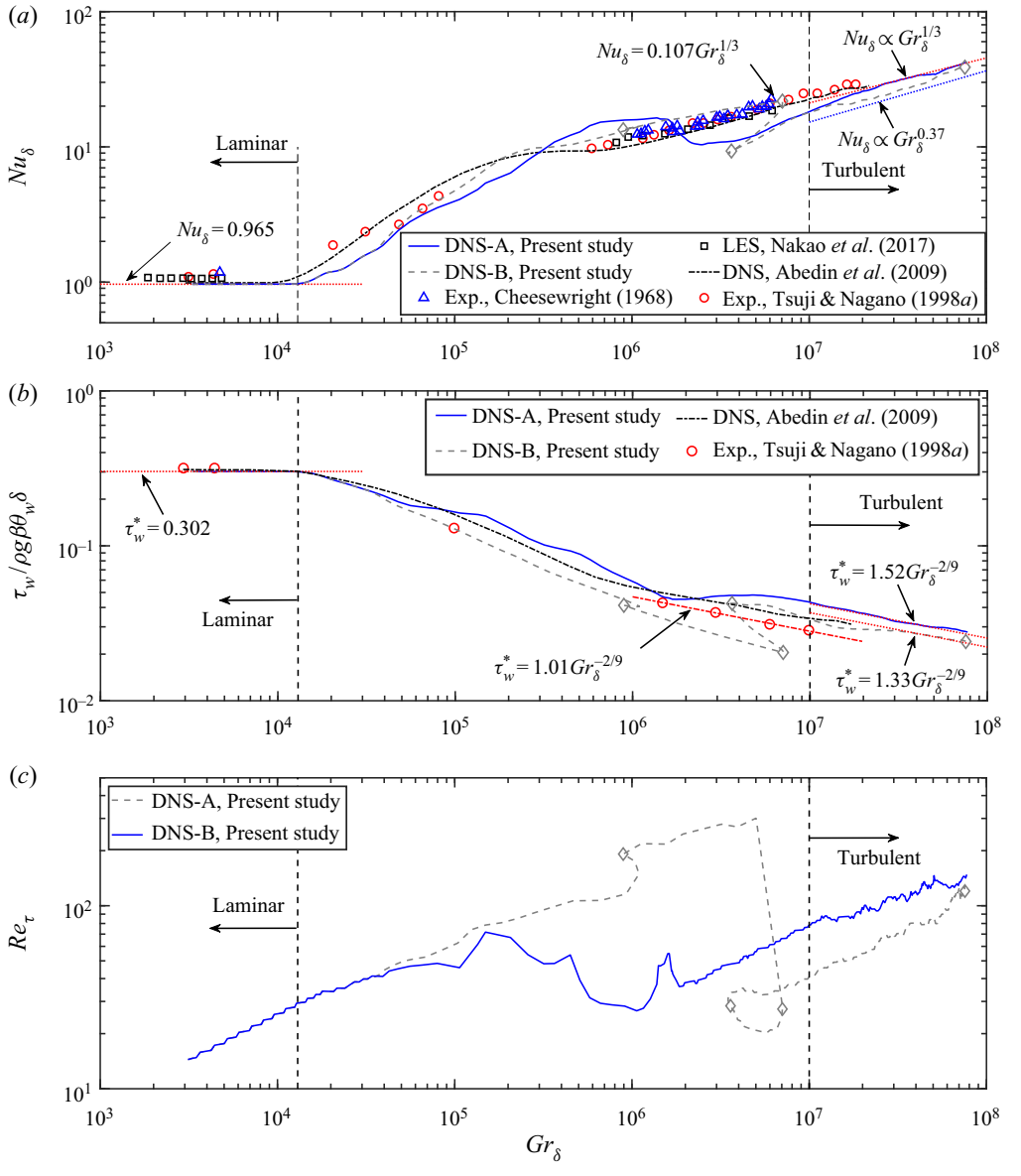

FIGURE 5. Temporal development of the wall characteristics: (*a*) Nusselt number; (*b*) wall shear stress; (*c*) the friction Reynolds number. The grey diamond symbols represent the data points shown in figure 2 for DNS-B.

the wall shear stress and the Nusselt number are found to follow the empirical formula,

$$Nu_\delta = 0.107Gr_\delta^{1/3}, \quad \tau_w^* = 1.01Gr_\delta^{-8/35.7} \approx 1.01Gr_\delta^{-2/9}. \tag{4.3a,b}$$

However, the temporally developing NCBL at $Gr_\delta \sim 10^6$ is not yet turbulent for the present study. For case DNS-B, two 'reversed' Grashof number regions, in which the Gr_δ gradually reduces, can be observed at $Gr_\delta \sim 10^6$ and $Gr_\delta \sim 7 \times 10^6$. These unusual reverses in Gr are found to be closely related to the pathway of the laminar–turbulent transition (the

aforementioned detachment of the convective rolls in figure 2) as Gr_δ is given by the shape of the velocity profile in the laminar–turbulent transition process (Ke *et al.* 2018). Nevertheless, at $Gr_\delta > 10^7$ the Nusselt number for the temporal cases start to share a similar exponential correlation as the empirical formula for the spatially developing NCBL with a different constant, such that

$$Nu_\delta = K_q Gr_\delta^{1/3}, \tag{4.4}$$

where $K_q = 0.098$ for case DNS-A, while DNS-B has $K_q = 0.085$ for $1.0 \times 10^7 < Gr_\delta < 5.0 \times 10^7$ but appears to converge to $K_q = 0.098$ over $5.0 \times 10^7 < Gr_\delta < 7.6 \times 10^7$. In a more recent study, Ng *et al.* (2017) obtained the empirical scaling

$$Nu_\delta \sim Gr_\delta^{0.37}, \tag{4.5}$$

by conditionally averaging on high wall shear events in their DNS of natural convection in a vertical differentially heated slot. The authors show that their empirical scaling relation given in (4.5) is consistent with the 1/2-power-law scaling with a logarithmic correction in homogeneous Rayleigh–Bènard convection, where the boundary layer is dominated by the bulk thermal convection (ultimate regime when Gr_δ is asymptotically high) in the sense of Grossmann & Lohse (2000, 2011). The difference between (4.4) and (4.5) is somewhat subtle in the current Gr_δ range of Nu_δ results shown in figure 5 (up to $Gr_\delta \sim 7.7 \times 10^7$ for DNS-A and $Gr_\delta \sim 7.6 \times 10^7$ for DNS-B). The temporal nature of our DNS means turbulence shows up in the instantaneous Nu_δ which makes detecting small changes in the Nu_δ–Gr_δ scaling without a large Gr_δ range difficult. Using empirical relationships for forced boundary layers, Wells & Worster (2008) showed that at very high Gr_δ the spatially developing vertical NCBL may attain a $Nu_\delta \sim Gr_\delta^{1/2}$ scaling which for the present flow is estimated above $Gr_\delta \sim O(10^{10})$. In the current Gr_δ range, we do not yet see evidence for $Nu_\delta \sim Gr_\delta^{1/2}$ in our Nu_δ results shown in figure 5(*a*).

Similar behaviour can also be found in the wall shear stress: the temporal cases start to follow the empirical exponential correlation with larger constants at $Gr_\delta > 10^7$,

$$\tau_w^* = K_\tau Gr_\delta^{-8/35.7} \approx K_\tau Gr_\delta^{-2/9}, \tag{4.6}$$

where $K_\tau = 1.52$ for case DNS-A and $K_\tau = 1.33$ for case DNS-B. Notably, the temporal DNS of Abedin *et al.* (2009) also indicates a larger constant for wall shear than the empirical correlation. Since the wall characteristics of the temporally developing NCBL exhibit similar scaling relations to the turbulent spatially developing NCBL at $Gr_\delta > 10^7$, we therefore refer to this regime as the turbulent regime for the temporally developing NCBL. The collapse of the wall characteristics in the turbulent regime indicate the NCBL obtained in DNS-A and DNS-B are, in some sense, initial condition-invariant: although the flow in DNS-B undergoes a weakly three-dimensional transition due to the difference in the initial condition, it still shares common features that can also observed in DNS-A in the turbulent regime – with a different constant. This can also be seen in figure 5(*c*) where the Re_τ for DNS-B is approaching the Re_τ in DNS-A as the Gr_δ increases. For clarity we present the results of DNS-A in the following sections unless otherwise specified. A detailed comparison of DNS-A and DNS-B will be given in § 6.4.

5. Profiles in the laminar-like sublayer

The mean temperature gradient in the slowly time-varying region can be obtained by integrating (3.4*b*) such that

$$\mathcal{C} \sim \frac{1}{Pr}\frac{\partial \theta^+}{\partial y^+} - (\overline{v'\theta'})^+, \tag{5.1}$$

where $\mathcal{C}$ is a constant resulting from performing the integration. In the close vicinity of the wall, (5.1) can be further simplified provided the turbulent transport $(\overline{v'\theta'})^+$ in this region is negligible, so that

$$\theta^+ \sim \mathcal{C}Pry^+ + \mathcal{D}, \tag{5.2}$$

is obtained after integrating (5.1) along the wall-normal direction. Here, $\mathcal{D}$ is also a constant resulting from performing the integration. Employing the boundary condition at $y^+ = 0$, $\theta^+ = 0$ and $(1/Pr)(\partial\theta^+/\partial y^+) = q_w^+$, the near-wall temperature profile is obtained as

$$\theta^+ = Pry^+. \tag{5.3}$$

This suggests that the mean temperature follows a linear relation in the close vicinity of the wall for the temporally developing NCBL, as reported by several NCBL studies (Tsuji & Nagano 1988; Hölling & Herwig 2005; Ng *et al.* 2017). Similarly, by assuming a slowly varying flow and neglecting the Reynolds shear stress in this region, the mean velocity profile is dominated by the buoyancy force in the region and can be obtained by integrating (3.4*a*) twice in the wall-normal direction, giving

$$u^+ \sim \iint -(Ri_w - Ri_\tau\theta^+)\,\mathrm{d}y^+\,\mathrm{d}y^+. \tag{5.4}$$

The temperature coupling term, θ^+, in (5.4) is then replaced by the linear relation (5.3). After applying the boundary conditions at the wall ($y^+ = 0$), i.e. $u^+ = 0$ and $\partial u^+/\partial y^+ = \tau_w^+$, gives

$$u^+ = y^+ - \frac{1}{2}Ri_w y^{+2} + \frac{Pr}{6}Ri_\tau y^{+3}, \tag{5.5}$$

in the near-wall region. Unlike the mean temperature profile, the mean velocity profile for the NCBL does not feature a linear region, as is commonly found in the viscous sublayer for the momentum-dominated flows. This is due to the presence of the extra buoyancy terms. The coefficients Ri_w and Ri_τ clearly indicate the Gr_δ-dependency of the mean streamwise velocity profile. Such modification of the mean profile takes a similar form to the pressure gradient effect described by Nickels (2004) for wall bounded flows subjected to large pressure gradients. The existence of two Richardson numbers is a result of the two temperature scales in the problem: Ri_w represents the bulk temperature difference $\theta_w = T_w - T_\infty$ which provides the driving force for buoyancy and Ri_τ indicates a wall heat flux quantity θ_τ which scales the near-wall temperature gradients. A similar analysis can also be seen in Hölling & Herwig (2005), where they have used the temperature gradients to identify the characteristic velocity, so that the buoyancy dependency is absorbed into the normalized coordinates. The near-wall mean profiles obtained here, given in (5.3) and (5.5), are consistent with the result Tsuji & Nagano (1988) obtained using a Taylor series expansion and the solution by Wells & Worster (2008) for spatially developing NCBLs.

Figure 6 shows the near-wall mean temperature and velocity profiles in wall units from the DNS data. The mean temperature θ^+, according to figure 6(*a*), shows a linear relationship in the near-wall region, as described by (5.3) for $y^+ < 5$. However, according

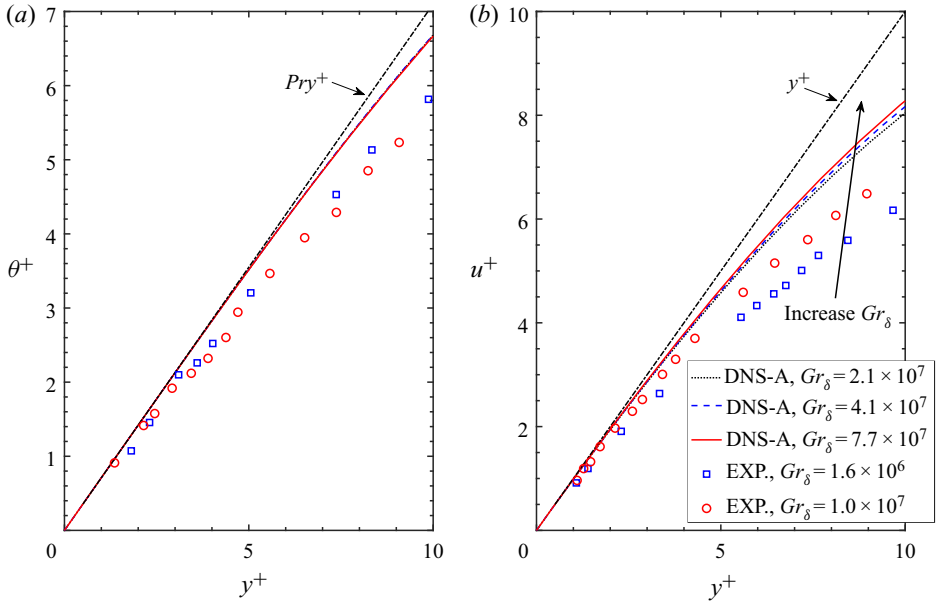

FIGURE 6. (*a*) Mean temperature profiles for the turbulent NCBL at different Gr_δ; (*b*) mean velocity profiles for the turbulent NCBL at different Gr_δ; the markers represents the experimental measurements of Tsuji & Nagano (1988) for a spatially developing NCBL with $Pr = 0.71$.

to figure 6(*b*), the viscous sublayer that is commonly found in the momentum-dominated flows in which region the linear relation

$$u^+ = y^+, \tag{5.6}$$

holds does not exist in the NCBL, as predicted by (5.5). A similar observation is also made by Tsuji & Nagano (1988) for a spatially developing NCBL, and Ng *et al.* (2017) for a differentially heated NCBL channel flow. From (5.5), the absence of the linear velocity profile (5.6) for the NCBL in the near-wall region is essentially due to the extra buoyancy, which can be seen in figure 7 where the buoyancy contribution to the mean velocity profile is shown in wall units. From figure 7, it is clear that the buoyancy contribution is negative and gradually approaches to zero as the flow reaches higher Gr_δ. The physical interpretation is rather simple: as the flow progressively achieves higher Gr_δ in the turbulent regime, the friction velocity u_τ is gradually growing in magnitude due to the increase in the wall shear stress τ_w. According to (4.4) and (4.6), the friction velocity u_τ and the wall heat flux q_w in the turbulent regime follow the scaling relation

$$u_\tau = K_\tau^{1/2}(g\beta\theta_w\nu)^{1/3}Gr_\delta^{1/18}, \tag{5.7a}$$

$$q_w = K_q(g\beta)^{1/3}\theta_w^{4/3}\rho C_p\kappa\nu^{-2/3}. \tag{5.7b}$$

It can be seen the wall heat flux q_w in the turbulent regime is a constant (independent of Gr_δ), suggesting the friction Richardson numbers depend solely on the friction velocity (or, the wall shear), such that

$$Ri_w \sim \frac{1}{u_\tau^3} \sim Gr_\delta^{-1/6}, \quad Ri_\tau \sim \frac{1}{u_\tau^4} \sim Gr_\delta^{-2/9}. \tag{5.8a,b}$$

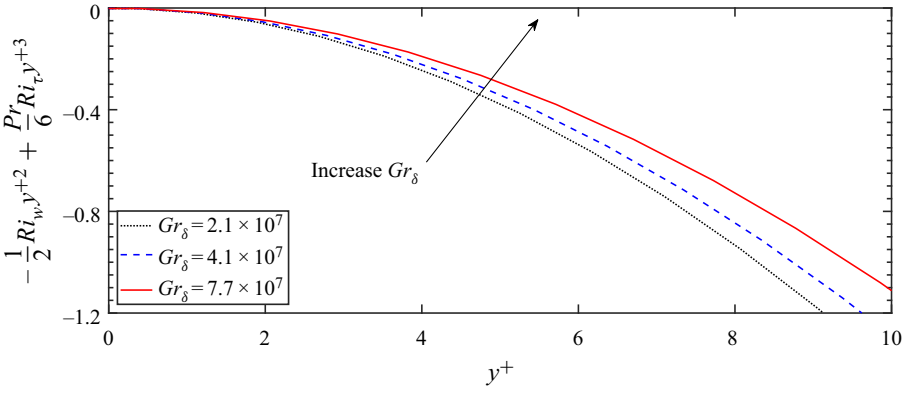

FIGURE 7. Buoyancy contribution to the mean velocity profile in wall units.

The buoyancy contribution thus asymptotically approaches zero,

$$-\frac{1}{2}Ri_w y^{+2} + \frac{Pr}{6}Ri_\tau y^{+3} \sim 0, \tag{5.9}$$

at some large u_τ (or, identically, large Gr_δ). Figure 8 depicts the development of the friction Richardson numbers. It can be seen that both Ri_w and Ri_τ qualitatively agree with the empirical correlation (5.8*a*,*b*) in the turbulent regime.

Further justification can be obtained by restarting the NCBL DNS-A in the turbulent regime, but having the temperature field uncoupled from the velocity field. The uncoupling of the temperature field is achieved by removing the buoyancy forcing term $\theta\delta_{i1}$ from the governing equation (2.1*b*) so that the temperature now acts as a passive scalar and the flow is completely dominated by the momentum. One may consider the uncoupled flow as a planar jet flow adjacent to the wall with an initial velocity profile taken from that of a turbulent NCBL. Figure 9 shows the comparison of the near-wall mean velocity profiles of the two flows. The near-wall mean velocity profile of the turbulent NCBL, according to figure 9, has an excellent agreement with (5.5) for $y^+ < 5$, beyond which point the turbulent transport becomes non-negligible; whereas the uncoupled case quickly recovers and matches the linear relation (5.6) for $y^+ < 5$ since the buoyancy effect is absent. This can be seen from the inset of figure 9, where the ratio u^+/y^+ at $y^+ = 5$ increases from 93.5 % (which is given by the NCBL profile as initial condition) to 98.6 % at $t^+ = 7.1$ and remains around 99 % subsequently.

6. The logarithmic region

Further away from the wall, a logarithmic region, where

$$\theta^+ = \frac{Pr_t}{K_v}\ln(y^+) + B_\theta, \tag{6.1}$$

can be found for the mean temperature profile for $y^+ > 50$ in figure 10(*a*). Here, Pr_t is the turbulent Prandtl number, K_v is the von Kármán constant and B_θ is a universal constant. Similar observations of the near-wall temperature structures are also made by the experimental measurements of a spatially developing turbulent NCBL (Tsuji & Nagano 1988), where they identified the logarithmic region to be $30 < y^+ < 200$ for

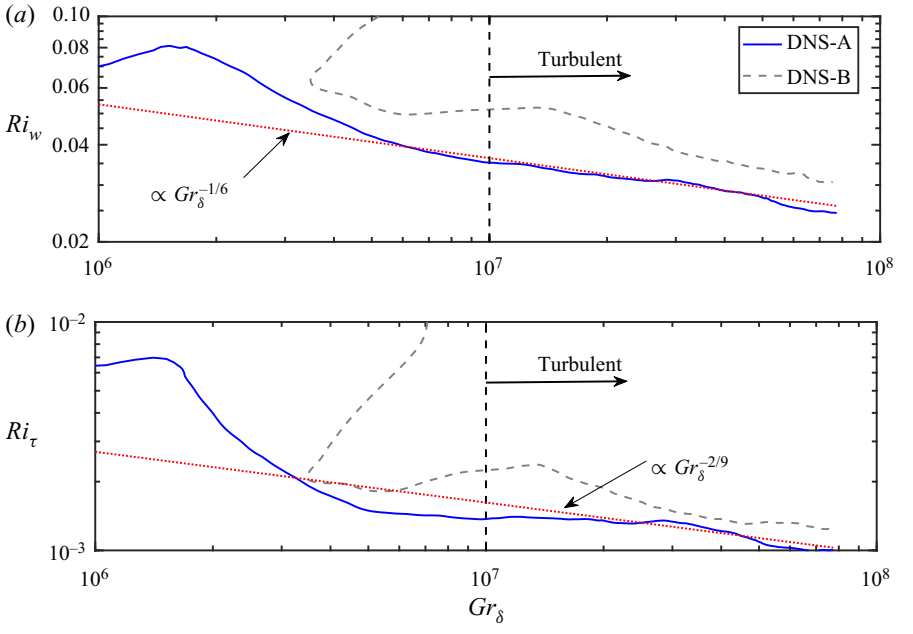

FIGURE 8. Development of the friction Richardson numbers with Gr_δ: (*a*) Ri_w; (*b*) Ri_τ.

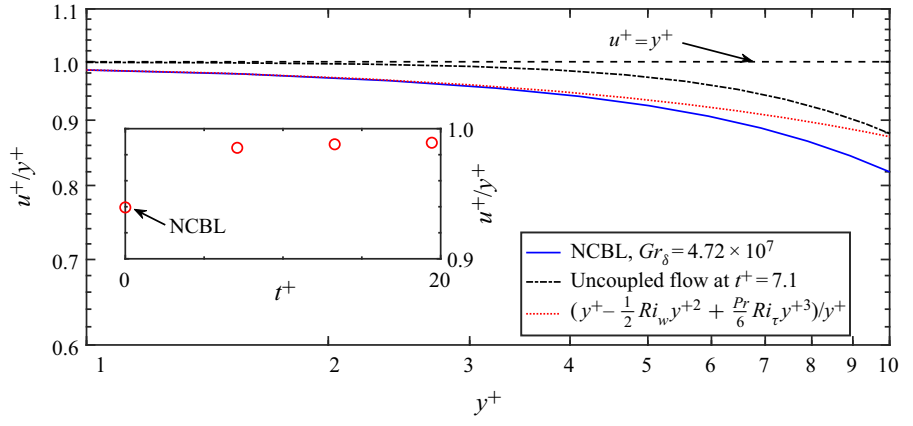

FIGURE 9. Comparison of the near-wall mean velocity profile of the NCBL and the temperature field uncoupled flow; the uncoupled flow uses the NCBL at $Gr_\delta = 4.72 \times 10^7$ as an initial condition ($t^+ = 0$). Inset shows the temporal development of u^+/y^+ at $y^+ \sim 5$ for the uncoupled flow.

Grashof number up to $Gr_\delta = 1 \times 10^7$ and the constant to be $Pr_t/K_v = 1.45$. However, we have adopted the same constants as Yaglom (1979) and Ng *et al.* (2017) for better agreement with our numerically generated data, i.e. $Pr_t = 0.85$ and $K_v = 0.41$. According to the spatially developing experiment by Tsuji & Nagano (1988), the constant B_θ appears to depend on, and vary with Gr_δ; whereas from figure 10(*a*), it can be seen that the temperature profiles agree well with (6.1) in the logarithmic region with the constant

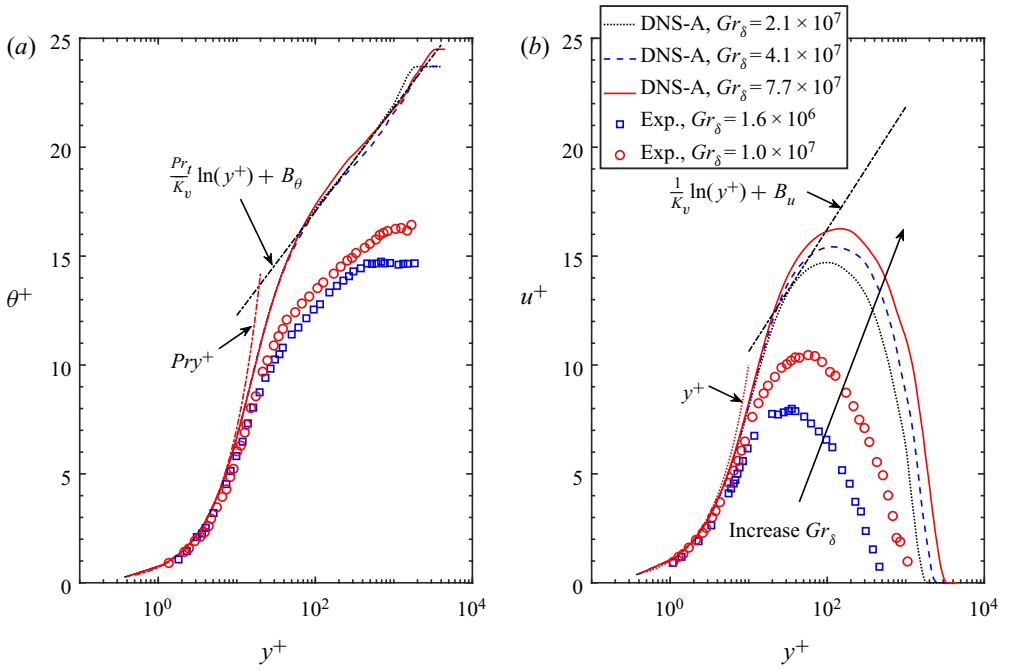

FIGURE 10. (*a*) Mean temperature profiles for the turbulent NCBL at different Gr_δ. (*b*) Mean velocity profiles for the turbulent NCBL at different Gr_δ; with $K_v = 0.41$, $Pr_t = 0.85$, $B_\theta = 7.5$ and $B_u = 5$. The markers represents the experimental measurements of Tsuji & Nagano (1988) for a spatially developing NCBL with $Pr = 0.71$.

$B_\theta = 7.5$, regardless of the value of Gr_δ. However, it should be noted that the data from Tsuji & Nagano (1988) are at relatively low Gr_δ when compared with the current study.

The mean velocity profiles, however, as shown in figure 10(*b*), demonstrate a strong Gr_δ dependency. From figure 10(*b*), the conventional log-law region, given by

$$u^+ = \frac{1}{K_v}\ln(y^+) + B_u, \tag{6.2}$$

cannot be observed for the NCBL even at $Gr_\delta = 7.7 \times 10^7$. Here, $B_u = 5$ is a constant for the results presented. The difference between the velocity profiles and the conventional log-law (6.2) becomes more significant with increasing Gr_δ as the velocity profiles grow in magnitude and do not exhibit a log-law region in the classical sense. Note the maximum velocity u_m^+ is also increasing with Gr_δ (or Re_τ) since the characteristic velocity u_τ does not contain any buoyancy information. A direct consequence is that the difference here (between the velocity profiles and the conventional log-law) is somewhat different from the overshoot of the conventional log-law in the sense of Nickels (2004) and Chan *et al.* (2015) due to low Re_τ effects. The above observation is consistent with previously reported behaviour (Tsuji & Nagano 1988; Ng *et al.* 2017). The absence of the conventional log-law for the velocity profile is not surprising as (6.2) does not take the buoyancy effect into account. We hereby propose a modified velocity profile prediction for the NCBL in the conventionally thought log-law region (where the flow varies slowly in time in the sense of figure 4 and the temperature has a log-law profile, $50 < y^+ < 150$ for our results at $Gr_\delta = 7.7 \times 10^7$) by taking the buoyancy effect into consideration. The mean velocity

profile in this region is obtained by integrating the velocity gradient, which can be solved from (3.11*a*) given the temporal derivative is zero. However, the Reynolds stress and the buoyancy force in (3.11*a*) are not yet analytically known and thus require appropriate modelling.

6.1. *Buoyancy force approximation*

The buoyancy force F_b^+ is fully described by the temperature profile θ^+ as follows:

$$F_b^+ \equiv \int_0^{y^+} (Ri_w - Ri_\tau \theta^+)\,\mathrm{d}y^+ = Ri_w y^+ - Ri_\tau \int_0^{y^+} \theta^+\,\mathrm{d}y^+, \tag{6.3}$$

since Ri_w and Ri_τ are both constants at a given Gr_δ. In the present study, the buoyancy force given in (6.3) is approximated by two approaches to simplify the analysis.

6.1.1. *Log-law approximation*

From figure 10(*a*), the temperature profile follows the log-law relation (6.1). Upon integration of (6.3) with respect to y^+ after the substitution of (6.1), the buoyancy force in the temperature log-law region can therefore be approximated by

$$F_b^+ = C_1 y^+ + Ri_\tau K_1 - Ri_\tau \frac{Pr_t}{K_v} \ln(y^+) y^+, \tag{6.4}$$

where the proportionality coefficient C_1 is given by

$$C_1 = Ri_w - Ri_\tau \left(B_\theta - \frac{Pr_t}{K_v} \right) \tag{6.5}$$

and K_1 is an unknown constant from integration. A similar approximation for the buoyancy force has also been applied by Wei (2019) to approximate the Reynolds shear stress in the differentially heated vertical channel NCBL flows. Empirically, by fitting (6.4) with the DNS data at $y^+ = 50$ (see figure 11), we have found

$$K_1 = 150, \tag{6.6}$$

is a constant for the Gr_δ range presented in the turbulent regime. As shown in figure 11, the integral constant K_1 sets the magnitude (vertical shift) of the buoyancy force when multiplied by Ri_τ in (6.4) at different Gr_δ. Our results suggest that K_1 does not have Gr_δ dependency since the temperature profiles in DNS-A are self-similar: we will show later in § 6.4 that for the non-self-similar temperature profiles in DNS-B and the spatially developing measurements of Tsuji & Nagano (1988) K_1 gradually approach to the constant obtained here by DNS-A as the flow achieves higher Gr_δ.

6.1.2. *Linear approximation*

The approximation of the buoyancy force (6.3) can be further simplified due to the fact that the θ^+ is changing only slightly in the temperature log-law region ($y^+ > 50$).

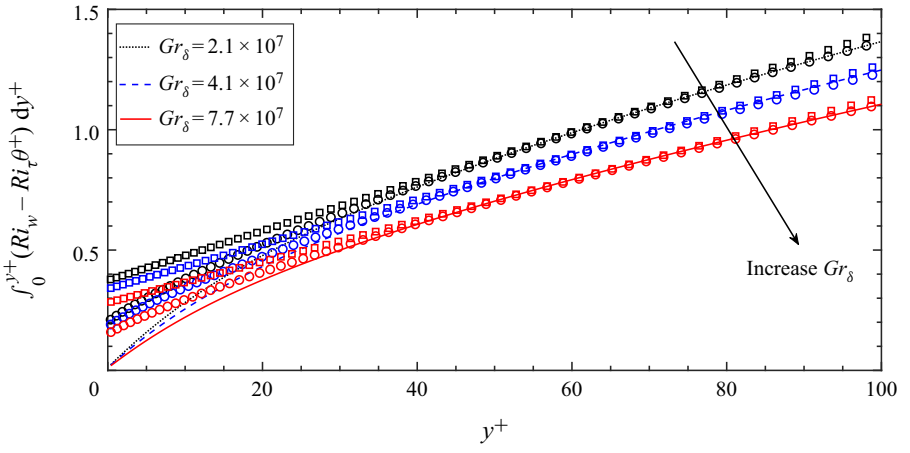

FIGURE 11. Comparison of the approximations of the buoyancy force at $Gr_\delta = 2.1 \times 10^7$, $Gr_\delta = 4.1 \times 10^7$ and $Gr_\delta = 7.7 \times 10^7$; lines show the DNS data; circle markers show the approximations by (6.4) with $K_1 = 150$; square markers show the approximations by (6.7).

By treating θ^+ as a constant in the temperature log-law region, (6.3) becomes

$$F_b^+ = C_2 y^+ + A_2, \tag{6.7}$$

where C_2 is a proportionality coefficient given by

$$C_2 = Ri_w - Ri_\tau \Theta^+ \tag{6.8}$$

and the intercept A_2 is given by

$$A_2 = K_2 Ri_\tau, \tag{6.9}$$

where K_2 is an unknown constant representing the difference between the linear approximation (6.7) and the nonlinear growth of the buoyancy force before the log-law region. Empirically, by matching the DNS data with (6.7) at $y^+ = 50$ we have found

$$K_2 = 280, \tag{6.10}$$

for the data shown. Here, Θ^+ is the mean value of θ^+ in the region. In the present study, $\Theta^+ = 16$ is used (see the temperature profiles in figure 10). Similar to K_1, the constants K_2, B_θ and Θ^+ obtained here appear universal in our Gr_δ range due to the self-similar temperature profiles in DNS-A. Evidently, when multiplied by Ri_τ, the constant K_2 also accounts for the Gr_δ dependency (see figure 11). The buoyancy force modelled by the linear relation (6.7) therefore depends solely on the wall characteristics since the proportionality coefficient C_2 and the intercept A_2 varies with Ri_w and Ri_τ only.

Figure 11 shows the comparison of the approximation of the buoyancy force given by (6.4) and (6.7) with the DNS data at different Gr_δ. According to figure 11, the buoyancy force F_b^+ decreases with increasing Gr_δ due to the increasing friction velocity u_τ. Both (6.4) and (6.7) show good agreement with the DNS data in the temperature log-law region $y^+ > 50$. The agreement between the approximations and the actual DNS data improves with increasing Gr_δ.

6.2. *Reynolds stress approximation*

In conventional momentum-dominated wall-bounded flows, the local momentum transfer by the Reynolds shear stress is frequently modelled by the Prandtl mixing length model (Prandtl 1925),

$$-(\overline{u'v'})^+ = l_m^{+2}\left(\frac{\partial u^+}{\partial y^+}\right)^2, \tag{6.11}$$

where l_m^+ is the mixing length. The presence of the wall, according to Townsend (1976), imposes a turbulent length scale on the velocity field so that the main eddies of the flow are, in a sense, 'attached' to the wall. In other words, the turbulent length scale of the large eddies (Townsend 1961),

$$L \equiv \frac{k^{3/2}}{\varepsilon}, \tag{6.12}$$

is expected to scale with the wall-normal distance y^+. Here, k and ε are the turbulent kinetic energy and the turbulent kinetic energy dissipation rate, respectively, defined by

$$k = \frac{1}{2}\overline{u_i'^2}, \quad \varepsilon = \nu\overline{\left(\frac{\partial u_i'}{\partial x_j}\right)^2}. \tag{6.13a,b}$$

Consequently, the mixing length is also expected to vary linearly with y^+ owing to the fact that the mixing length l_m^+ is proportional to L in the log-law region for $y^+ > 50$ (see, for example, Townsend 1961; Pope 2000, pp. 288–290), such that

$$L^+ = \frac{L}{l_\tau} \propto l_m^+ \propto y^+, \tag{6.14}$$

and the mixing length can be described by

$$l_m^+ = Dy^+, \tag{6.15}$$

where the proportionality coefficient D is known as the von Kármán constant K_v in the conventional momentum-dominated flows.

Since the NCBL is also bounded by the wall, it is convenient to assume the Reynolds shear stress shares a similar behaviour to the momentum-dominated flows and can be modelled by (6.11) and (6.15). The validity of applying (6.15) to the NCBL may be justified by examining the turbulent length scale L. As depicted in figure 12, the turbulent length scale L follows a linear relation with y^+ at sufficiently high Gr_δ (or, Re_τ) in the turbulent regime in the range $10 < y^+ < 100$, indicating a mixing length l_m^+ proportional to y^+ as given in (6.15). However, it should be noted that the coefficient D in (6.15) for NCBL remains unknown and may have a Gr_δ dependency. In the present study, the coefficient D is obtained empirically by rearranging (6.11),

$$D = \left[\frac{-(\overline{u'v'})^+}{(\partial u^+/\partial y^+)^2 y^{+2}}\right]^{1/2}. \tag{6.16}$$

According to figure 13, it can be seen that the ratio $-(\overline{u'v'})^+/(\partial u^+/\partial y^+)^2$ scales well with y^{+2} in the temperature log-law region for $y^+ > 50$ (see inset), and the coefficient D, with

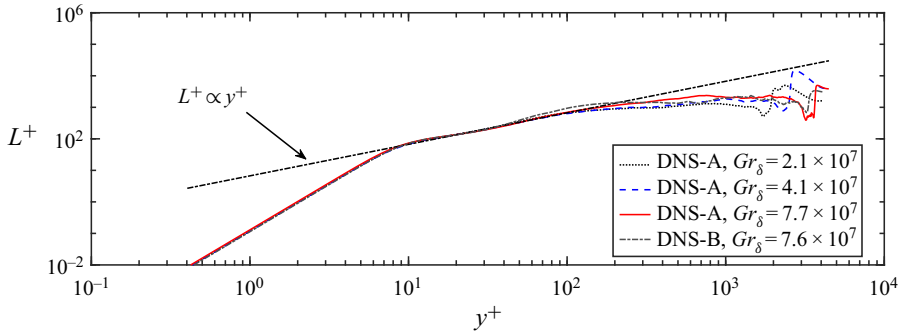

FIGURE 12. The turbulent length scale in wall unit L^+ against the wall-normal distance y^+ for DNS-A at $Gr_\delta = 2.1 \times 10^7$, $Gr_\delta = 4.1 \times 10^7$ and $Gr_\delta = 7.7 \times 10^7$; and for DNS-B at $Gr_\delta = 7.6 \times 10^7$.

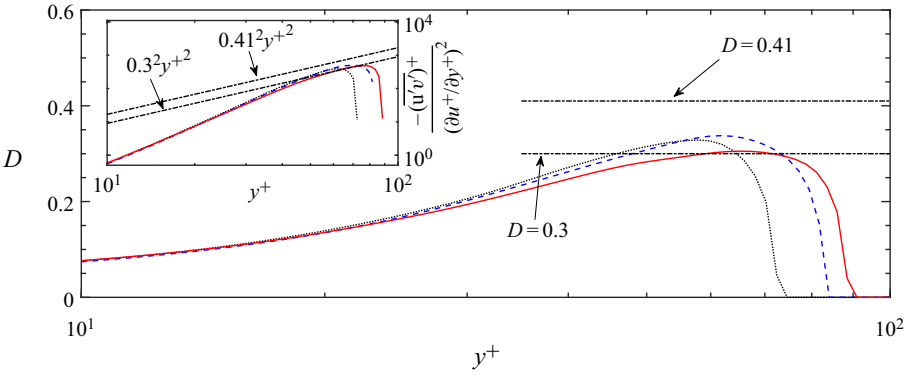

FIGURE 13. Proportionality coefficient D at different Gr_δ: black dotted, $Gr_\delta = 2.1 \times 10^7$; blue dashed, $Gr_\delta = 4.1 \times 10^7$; red solid, $Gr_\delta = 7.7 \times 10^7$. Inset shows the ratio $D^2 y^{+2} = -(\overline{u'v'})^+/(\partial u^+/\partial y^+)^2$.

this more sensitive measure (6.16), shows minimal Gr_δ-dependency in our Gr_δ range. Here, we choose

$$D = 0.3, \tag{6.17}$$

for the following analysis. It should be noted that the negative values of $-(\overline{u'v'})^+$ are prohibited by the nature of the mixing length model (6.11), we therefore shall only focus on the region where $-(\overline{u'v'})^+$ is positive (up to $y^+ \sim 90$ for $Gr_\delta = 7.7 \times 10^7$) in the present study.

6.3. *Modified log-law*

Making use of (6.11), the force balance equation (3.11*a*) can be rewritten as a quadratic equation about the velocity gradient $\partial u^+/\partial y^+$,

$$\frac{\partial u^+}{\partial y^+} + l_m^{+2}\left(\frac{\partial u^+}{\partial y^+}\right)^2 + F_b^+ = \tau_w^+. \tag{6.18}$$

The mean velocity gradient $\partial u^+/\partial y^+$ is therefore obtained as the solution to the quadratic equation (6.18). Note for NCBL, the velocity grows in the log-law region until it reaches its maximum and therefore a positive velocity gradient is expected,

$$\frac{\partial u^+}{\partial y^+} = \frac{-1 + [1 + 4l_m^{+2}(\tau_w^+ - F_b^+)]^{1/2}}{2l_m^{+2}}. \tag{6.19}$$

When the buoyancy force F_b^+ is absent (for momentum-dominated flows or when buoyancy force is negligible, i.e. $Gr_\delta \sim \infty$), (6.19) reduces to the ordinary velocity gradient equation for the conventional velocity log-law region in the momentum-dominated flows (see, for example, Buschmann & Gad-el Hak 2005). A similar method was also adapted by Granville (1989) and Buschmann & Gad-el Hak (2005) when deriving the velocity log-law region for the wall-bounded turbulent boundary layers. In their analysis a constant shear layer, where $\partial u^+/\partial y^+ - (\overline{u'v'}^+) = \tau_w^+$, is assumed, whereas in the present study the total force in the near-wall region is a constant as shown in figure 4(*b*).

Owing to the fact that the molecular shear stress is negligible in this region (see also, figure 4), (6.18) reduces to a more convenient form,

$$l_m^{+2}\left(\frac{\partial u^+}{\partial y^+}\right)^2 = \tau_w^+ - F_b^+. \tag{6.20}$$

With $\tau_w^+ = 1$, the buoyancy force F_b^+ in (6.20) is then replaced by the approximations given in § 6.1. By applying the logarithmic approximation (6.4), the velocity gradient is obtained as

$$\widehat{\frac{\partial u^+}{\partial y^+}} = \frac{\sqrt{1 - C_1 y^+ - Ri_\tau K_1 + Ri_\tau \dfrac{Pr_t}{K_v}\ln(y^+)y^+}}{Dy^+}. \tag{6.21}$$

Alternatively, by applying the linear approximation of the buoyancy force given in (6.7), (6.20) can be reduced to

$$\widetilde{\frac{\partial u^+}{\partial y^+}} = \frac{\sqrt{1 - C_2 y^+ - A_2}}{Dy^+}. \tag{6.22}$$

Note when Gr_δ asymptotically goes to infinity, both C_2 and A_2 go to zero due to large u_τ and (6.22) takes the form of the conventional momentum-dominated log-law region, i.e. $\partial u^+/\partial y^+ = 1/(Dy^+)$. Figure 14 compares the actual velocity gradient obtained by the DNS data with the predictions by (6.21) and (6.22). Both predictions show excellent agreement with the DNS data in the range $50 < y^+ < 90$ since the buoyancy force and the Reynolds shear stress are correctly approximated and modelled. The mean velocity profile is therefore obtained as

$$u^+ = \int_0^{y_c^+} \frac{\partial u^+}{\partial y^+}\,\mathrm{d}y^+ + \int_{y_c^+}^{y^+} \frac{\partial u^+}{\partial y^+}\,\mathrm{d}y^+, \tag{6.23}$$

where y_c^+ is the starting point of the log-law region for the velocity profile. In the present study, it is assumed that the velocity log-law region starts at the same location as the

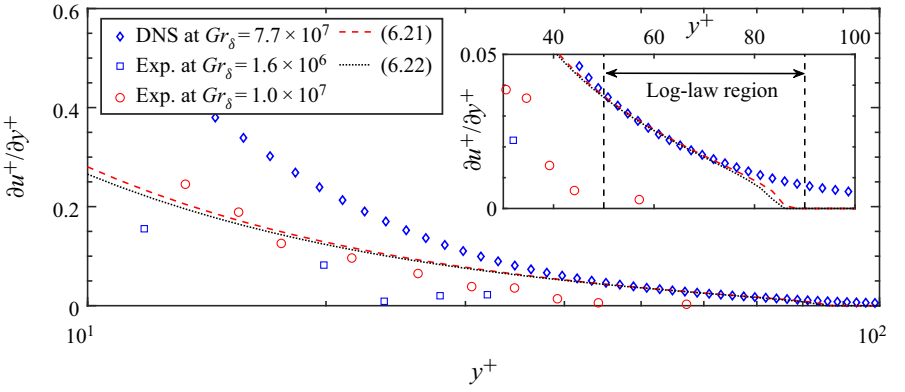

FIGURE 14. The mean velocity gradient obtained from DNS-A at $Gr_\delta = 7.7 \times 10^7$ and the predictions made by (6.21) and (6.22); with experimental measurements from Tsuji & Nagano (1988) for a spatially developing NCBL at lower Gr_δ. Inset shows an enlarged view near the modified log-law region.

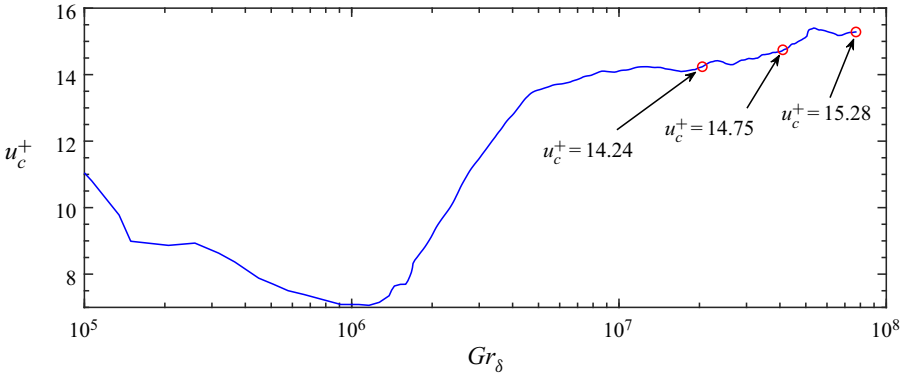

FIGURE 15. The development of the velocity magnitude u_c^+ (u^+ at $y^+ = 50$) against Gr_δ; the red circles mark the u_c^+ value used for $Gr_\delta = 2.1 \times 10^7$, $Gr_\delta = 4.1 \times 10^7$ and $Gr_\delta = 7.7 \times 10^7$, respectively.

temperature log-law region, i.e. $y_c^+ = 50$. Evidently, the first integration in (6.23) yields

$$\int_0^{y_c^+} \frac{\partial u^+}{\partial y^+}\,\mathrm{d}y^+ = u_c^+, \tag{6.24}$$

where u_c^+ is a constant given by the velocity magnitude at location $y^+ = y_c^+$. Recall that there is a buoyancy contribution in $y^+ < 50$, so the magnitude of u_c^+ is expected to depend on the wall characteristics, i.e. u_τ and θ_τ, and thus on Gr_δ, as demonstrated by figure 15.

The integrand in the second part of (6.23) can be replaced by (6.21) or (6.22). Unfortunately, (6.21) is analytically difficult to integrate. However, we are able to integrate (6.21) numerically to obtain the mean velocity profile, as shown in figure 16(*a*) along with the DNS data. As demonstrated by figure 16(*a*), the predictions made by (6.21) account for the Gr_δ effect (for example, the increasing magnitude of the velocity) and exhibit excellent agreement with the DNS data for $y^+ > 50$. However, beyond $y = 0.6\delta_m$ (equivalently, $y^+ = 60$ for $Gr_\delta = 2.1 \times 10^7$, $y^+ = 70$ for $Gr_\delta = 4.1 \times 10^7$ and $y^+ = 90$

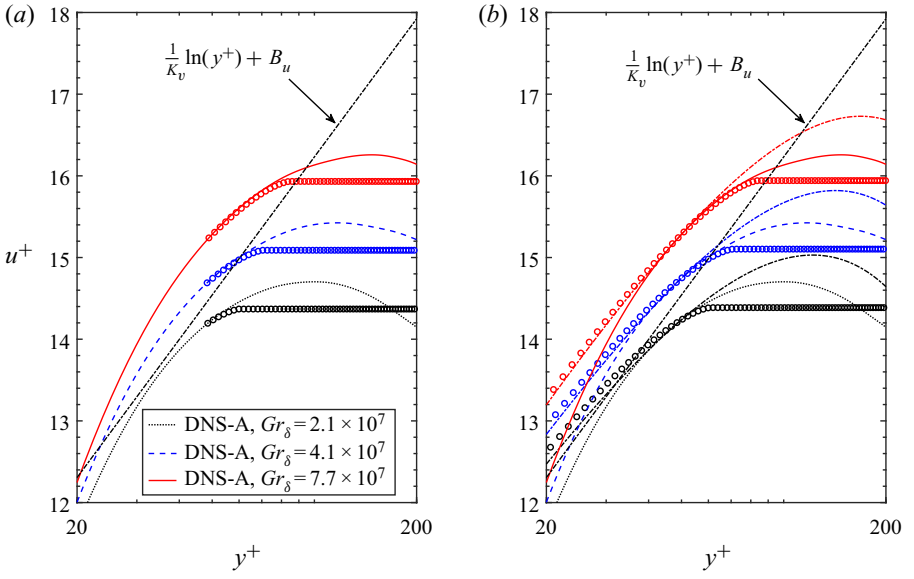

FIGURE 16. Mean velocity profiles of the turbulent NCBL in the temperature log-law region for case DNS-A: black dotted line, the conventional log-law given by (6.2). (*a*) Mean velocity profiles at different Gr_δ and predictions by numerically integrating (6.21) (circle markers); (*b*) mean velocity profiles at different Gr_δ and predictions by (6.25) (circle markers) and the modified log-law (6.29) (dash-dotted lines).

for $Gr_\delta = 7.7\times10^7$), the prediction by (6.21) no longer works as it is close to the velocity maximum location δ_m and the Reynolds stress $-(\overline{u'v'})^+$ becomes negative, requiring $l_m^{+2} < 0$ in the mixing length model, and the buoyancy force F_b^+ becomes larger than the wall shear stress τ_w^+, indicating $\tau_w^+ - F_b^+ < 0$ in (6.20).

On the other hand, making use of (6.22), (6.23) reduces to

$$u^+ = u_c^+ + \frac{\sqrt{1-A_2}}{D}\ln\left(\frac{1-\sqrt{1-C_2y^+-A_2}/\sqrt{1-A_2}}{1+\sqrt{1-C_2y^+-A_2}/\sqrt{1-A_2}}\right)+\frac{2}{D}\sqrt{1-C_2y^+-A_2}+E_1, \tag{6.25}$$

where E_1 is a parameter independent of y^+ from the definite integration, given by

$$E_1 = -\frac{\sqrt{1-A_2}}{D}\ln\left(\frac{1-\sqrt{1-C_2y_c^+-A_2}/\sqrt{1-A_2}}{1+\sqrt{1-C_2y_c^+-A_2}/\sqrt{1-A_2}}\right)-\frac{2}{D}\sqrt{1-C_2y_c^+-A_2}. \tag{6.26}$$

It is worth noting that E_1 varies with Gr_δ since the proportionality coefficient C_2 and intercept A_2 depends on Gr_δ.

The Puiseux series expansion of (6.25) at $y^+ = 0$ yields a modified velocity log-law,

$$u^+ \sim u_c^+ + \frac{\sqrt{1-A_2}}{D}\ln\left(\frac{C_2y^+}{4\sqrt{1-A_2}}\right)+\frac{2\sqrt{1-A_2}}{D}-\frac{C_2y^+}{2D\sqrt{1-A_2}}+E_2+O(y^{+2}), \tag{6.27}$$

where E_2 is a y^+-independent parameter from the definite integration, representing the difference between the logarithmic fit and the velocity magnitude at y_c^+ (for example,

intuitively, one would expect $u^+ = u_c^+$ at $y^+ = y_c^+$),

$$E_2 = -\frac{\sqrt{1-A_2}}{D}\ln\left(\frac{C_2 y_c^+}{4\sqrt{1-A_2}}\right) - \frac{2\sqrt{1-A_2}}{D} + \frac{C_2 y_c^+}{2D\sqrt{1-A_2}}. \tag{6.28}$$

As E_2 is a function of C_2 and A_2, it also has a Gr_δ-dependency. To compare with the conventional log-law, it is convenient to rewrite (6.27) as

$$u^+ \sim \underbrace{\frac{\sqrt{1-A_2}}{D}\ln(y^+)}_{\text{Logarithmic term}} + \underbrace{\frac{\sqrt{1-A_2}}{D}\left[\ln\left(\frac{C_2}{4\sqrt{1-A_2}}\right)+2\right] - \frac{C_2 y^+}{2D\sqrt{1-A_2}}}_{\text{Buoyancy effect on magnitude}} + \underbrace{E_2 + u_c^+}_{\text{Initial condition}}. \tag{6.29}$$

The first term in (6.29) shows the logarithmic relation between the wall-normal distance y^+ and the mean velocity u^+, although the slope is adjusted by the magnitude of the buoyancy in the log-law region. The buoyancy further affects the magnitude of the velocity by the extra terms that contain C_2 and A_2, as indicated by (6.29). Finally, the Gr_δ-dependent parameter E_2 and u_c^+ indicate the velocity information at the starting point of the log-law region. The resultant velocity prediction (6.25) and the modified log-law (6.29) are in a similar form to the mean velocity distribution in an equilibrium layer with a linear shear stress distribution given in Townsend (1961), where the slope of the logarithmic profile is adjusted by the wall shear stress instead of buoyancy and the buoyancy effect in (6.29) is replaced by the non-constant shear stress effect.

For the conventional momentum-dominated boundary layers (without buoyancy), the buoyancy effect on the velocity magnitude vanishes due to the absence of C_2 and K_2, and both u_c^+ and E_2 become independent of Re when the flow is turbulent enough (this is due to the fact that the velocity magnitude at the end of the viscous sublayer or buffer layer is independent of Re in the momentum-dominated flows since flow quantities in the close vicinity of the wall scale with the viscous scales ν and u_τ), so that they combine to give the constant offset

$$B_u = u_c^+ + E_2 \sim 5. \tag{6.30}$$

Consequently, this results in the conventional log-law given in the form of (6.2). In contrast, from (6.29), the shape of the velocity profile is adjusted by the buoyancy force in a complex manner, whilst the magnitude of the velocity relies on the Gr_δ-dependent initial condition u_c^+ and E_2 (or E_1 in (6.25)). As depicted by figure 16(*b*), the modified log-law region expands as Gr_δ increases and the predictions made by (6.25) and (6.29) show relatively good collapse on the DNS data in this region.

6.4. *Comparison with DNS-B and spatially developing NCBL*

Direct application of (6.29) with the constants obtained from DNS-A ($K_1 = 150$, $K_2 = 280$, $\Theta^+ = 16$ and $B_\theta = 7.5$) to DNS-B does not show such a good agreement as DNS-A. This is because the temperature profile of DNS-B, as shown in figure 17, has not yet reached fully developed conditions and demonstrates a Gr_δ dependence – the temperature distribution and the resultant buoyancy force in DNS-B are not yet self-similar. The Gr_δ dependence here is a proxy for development time. The Gr_δ (or time t) taken for DNS-A and DNS-B to reach self-similar conditions are quite different due to the difference in initial conditions. The logarithmic fit (6.1) for the temperature profile of DNS-B suggests the constant B_θ and the average temperature in the log-law region Θ^+ are both Gr_δ dependent

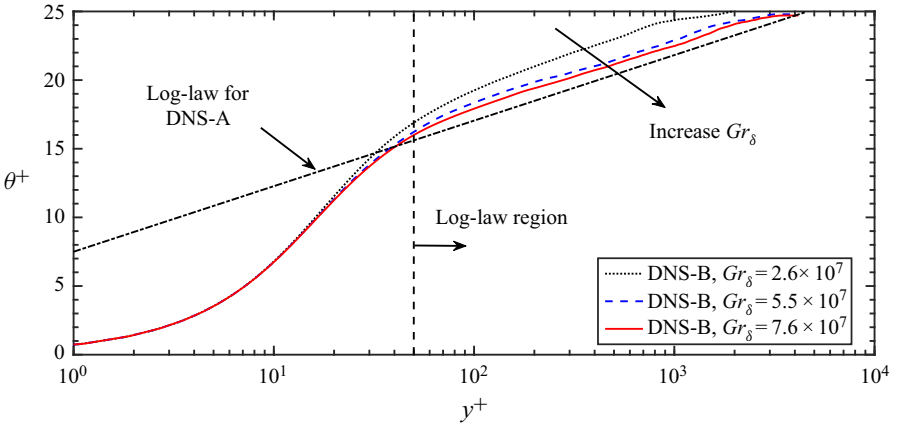

FIGURE 17. The mean temperature profiles for the turbulent NCBL at different Gr_δ for DNS-B.

Dataset	Gr_δ	Pr_t/K_v	B_θ	Θ^+	K_1	K_2	u_c^+
DNS-B	2.6×10^7	2.07	10	18	235	335	13.67
DNS-B	5.5×10^7	2.07	8.7	17.5	190	330	14.51
DNS-B	7.6×10^7	2.07	8.3	17	165	305	14.87
DNS-A	Universal	2.07	7.5	16	150	280	figure 15
Exp.	1.0×10^7	1.45	6.8	12	120	250	10.02
Exp.	1.6×10^6	1.45	6	11	80	60	7.87

TABLE 3. Grashof number dependent constants used in the modified log-law (6.29) for DNS-B and the experimental measurements from Tsuji & Nagano (1988).

(values are listed in table 3). The absence of the self-similar temperature profile in DNS-B implies that the constants associated with buoyancy force in (6.4) and (6.7) must be modified. This can be achieved by replacing the universal constants in DNS-A with the local values listed in table 3 when modelling the buoyancy force in (6.4) and (6.7). It appears a reasonable approach as the buoyancy force F_b is essentially determined by the local temperature profile. We show in figure 18 that once these constants are modified, the prediction shows excellent agreement with DNS-B in the log-law region ($y^+ > 50$). The length of the log-law region increases as the flow achieves a higher Gr_δ in DNS-B. At $Gr_\delta = 7.6\times10^7$, the log-law region extends up to $y^+ = 70$ as the Reynolds shear stress $-\overline{u'v'}$ becomes negative at $y^+ = 70$ (see, e.g. figure 4).

Similar to DNS-B, the experimental measurements by Tsuji & Nagano (1988) also show a strong Gr_δ dependence (see, e.g. figure 10*a*). By empirically adjusting constants for the local temperature profile (see table 3), predictions made by the modified log-law show qualitative agreement with the experimental measurements, as shown in figure 19. Note that $y_c^+ = 30$ is used for the experiment data as Tsuji & Nagano (1988) have identified the starting point for the temperature log-law region at $y^+ = 30$. At $Gr_\delta = 1.6\times10^6$, the modified log-law region does not seem to exist as the NCBL is at a relatively low Gr_δ, and the velocity maximum (at $y^+ \sim 35$) is located very close to $y_c^+ = 30$. At $Gr_\delta = 1.0\times10^7$, the modified log-law region starts to appear and the prediction made by (6.29) agrees

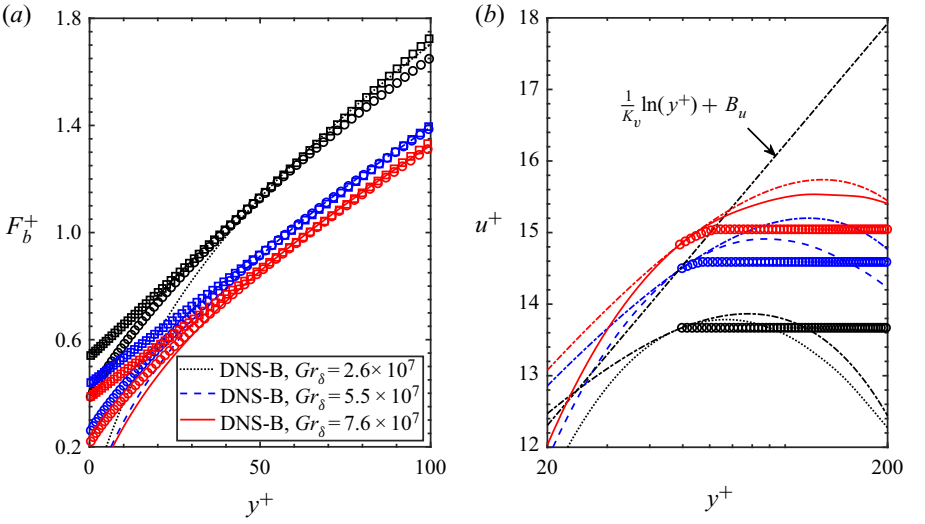

FIGURE 18. The application of the modified log-law to DNS-B using local constants: (*a*) buoyancy force at different Gr_δ and predictions by (6.4) (circle markers) and (6.7) (square markers); (*b*) mean velocity profiles at different Gr_δ and predictions by (6.25) (circle markers) and the modified log-law (6.29) (dash-dotted lines); black dotted line shows the conventional log-law given by (6.2).

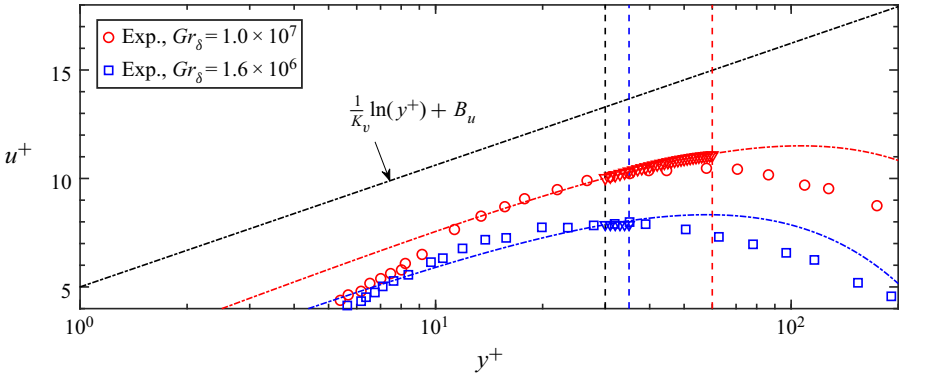

FIGURE 19. The application of the modified log-law to the spatially developing NCBL measured by Tsuji & Nagano (1988); predictions made by numerically integrating (6.21) are shown in triangle symbols; predictions made by the modified log-law (6.29) are shown in dash-dotted lines; the vertical dashed lines show the start of the log-law region (black), the maximum velocity location at $Gr_\delta = 1.6\times 10^6$ (blue) and the maximum velocity location at $Gr_\delta = 1.0\times 10^7$ (red).

with the experimental measurements in the range $30 < y^+ < 40$. The short log-law region may be due to the fact that the Gr_δ is not sufficiently high (recall figure 10, the constant B_θ in (6.1) still depends on Gr_δ for the measurements by Tsuji & Nagano 1988) and the starting point of the log-law region at $y_c^+ = 30$ is located close to the velocity maximum at $y^+ \sim 60$. Nevertheless, according to table 3, it can be seen that all the local constants are

Assumptions	F_b^+	$(\overline{u'v'})^+$	D	$\partial u^+/\partial y^+$	u^+
(6.1)	(6.4)	(6.11)	0.3	(6.19)	(6.23), obtained numerically
(6.1) and $\nu \sim 0$	(6.4)	(6.11)	0.3	(6.21)	(6.23), obtained numerically
(6.1), $\nu \sim 0$, $\theta^+ \sim \Theta^+$	(6.7)	(6.11)	0.3	(6.22)	(6.25)
(6.1), $\nu \sim 0$, $\theta^+ \sim \Theta^+$, Puiseux series expansion	(6.7)	(6.11)	0.3	(6.22)	Modified log-law, (6.29)

TABLE 4. Assumptions and modelling of the forces in the log-law region and the resultant velocity predictions.

approaching the universal values obtained in DNS-A with increasing Gr_δ for both DNS-B and the experimental measurements.

7. Concluding remarks

In the present study, the law of the wall has been investigated for the mean temperature and velocity profiles of a parallel temporally developing NCBL. The dependence of the turbulent statistics on the initial conditions are also investigated using two DNS. Although the two DNS undergo different laminar–turbulent transition mechanisms, they still share the same Gr_δ scaling relationship for Nu_δ and τ_w. By the end of the simulation, we have achieved $Gr_\delta = 7.7 \times 10^7$ which corresponds to $Re_\tau = 148$ for case DNS-A and $Gr_\delta = 7.6 \times 10^7$ which corresponds to $Re_\tau = 120$ for case DNS-B. Based on the DNS data, we have identified a constant flux layer in the near-wall region, similar to the observations in spatially developing NCBLs (George & Capp 1979; Hölling & Herwig 2005). A constant forcing layer which coincides with the constant flux layer was also identified for the first time using DNS. In this region, the Reynolds shear stress, molecular shear stress and the buoyancy force balances the shear stress on the wall. The two constant layers indicate the boundary layer is varying very slowly (i.e. the temporal evolution is negligible) in the near-wall region. In the close vicinity of the wall ($y^+ < 5$), the temperature profile expressed in wall units follows a linear relationship; whereas the velocity profile is modified by buoyancy forcing parallel to the wall, and only becomes asymptotic to a linear profile at very high Gr_δ, consistent with Ng *et al.* (2017). Further away from the wall, a logarithmic region is found for the temperature profile for $y^+ > 50$. According to the DNS data, the conventional log-law for the velocity profile does not hold for the NCBL as it does not account for the buoyancy. To predict the mean velocity profile in this region, we propose a modified log-law by taking the buoyancy force into consideration with varying levels of approximation. Such a log-law contributes towards a thorough understanding of the near-wall scaling, which provides useful information for the development of near-wall turbulence models and wall functions for buoyancy driven boundary layers (e.g. Kiš & Herwig 2012). The buoyancy effect for $y^+ > 50$ is found to be well approximated by a linear function of y^+, with the proportionality coefficient C_2 and the intercept A_2 being functions of Ri_w and Ri_τ. The Reynolds shear stress, however, is modelled by the mixing length model based on the observation that the mixing length scales linearly with distance from the wall, with $l_m^+ = Dy^+$.

A brief summary of the assumptions and the resultant velocity predictions proposed by the present study are listed in table 4. With the modelling of the buoyancy force and Reynolds shear stress, we compare the DNS results for two initializations and with

the spatially developing data of Tsuji & Nagano (1988). Although there is some flow dependence on the temperature profile, these differences decrease as Gr_δ increases. The Gr_δ dependency here is a result of the initial temperature profile after transition which may vary between studies and will reduce with time (temporally developing flow) or distance from the leading edge (spatially developing flow). Nevertheless, the modified log-law (6.29) appear to be both flow and Gr_δ independent in our study, except for u_c^+ which includes a buoyancy effect from the $y^+ < 50$ region in the flow for which we have no model. Validated against the DNS data, we have found the modified log-law (6.29) is able to provide the velocity prediction in the log-law region with reasonable accuracy given the shear stress and the heat flux on the wall.

Acknowledgements

The authors gratefully acknowledge the computational resources provided by the National Computational Infrastructure (NCI) Australia and by the University of Sydney high performance computing facility Artemis.

Declaration of interests

The authors report no conflict of interest.

REFERENCES

ABEDIN, M. Z., TSUJI, T. & HATTORI, Y. 2009 Direct numerical simulation for a time-developing natural-convection boundary layer along a vertical flat plate. *Intl J. Heat Mass Transfer* **52** (19–20), 4525–4534.

ABEDIN, M. Z., TSUJI, T. & HATTORI, Y. 2010 Direct numerical simulation for a time-developing combined-convection boundary layer along a vertical flat plate. *Intl J. Heat Mass Transfer* **53** (9–10), 2113–2122.

BUSCHMANN, M. H. & GAD-EL HAK, M. 2005 New mixing-length approach for the mean velocity profile of turbulent boundary layers. *Trans. ASME: J. Fluids Engng* **127** (2), 393–396.

CHAN, L., MACDONALD, M., CHUNG, D., HUTCHINS, N. & OOI, A. 2015 A systematic investigation of roughness height and wavelength in turbulent pipe flow in the transitionally rough regime. *J. Fluid Mech.* **771**, 743–777.

CHEESEWRIGHT, R. 1968 Turbulent natural convection from a vertical plane surface. *J. Heat Transf.* **90** (1), 1–6.

FUJII, T., TAKEUCHI, M., FUJII, M., SUZAKI, K. & UEHARA, H. 1970 Experiments on natural-convection heat transfer from the outer surface of a vertical cylinder to liquids. *Intl J. Heat Mass Transfer* **13** (5), 753–787.

GEORGE, W. K. & CAPP, S. P. 1979 A theory for natural convection turbulent boundary layers next to heated vertical surfaces. *Intl J. Heat Mass Transfer* **22** (6), 813–826.

GRANVILLE, P. S. 1989 A modified van driest formula for the mixing length of turbulent boundary layers in pressure gradients. *Trans. ASME: J. Fluids Engng* **111**, 94–97.

GROSSMANN, S. & LOHSE, D. 2000 Scaling in thermal convection: a unifying theory. *J. Fluid Mech.* **407**, 27–56.

GROSSMANN, S. & LOHSE, D. 2001 Thermal convection for large Prandtl numbers. *Phys. Rev. Lett.* **86** (15), 3316–3319.

GROSSMANN, S. & LOHSE, D. 2011 Multiple scaling in the ultimate regime of thermal convection. *Phys. Fluids* **23** (4), 045108.

HÖLLING, M. & HERWIG, H. 2005 Asymptotic analysis of the near-wall region of turbulent natural convection flows. *J. Fluid Mech.* **541**, 383–397.

HUTCHINS, N. & MARUSIC, I. 2007 Large-scale influences in near-wall turbulence. *Phil. Trans. R. Soc. Lond.* A **365** (1852), 647–664.

ILLINGWORTH, C. R. 1950 Unsteady laminar flow of gas near an infinite flat plate. *Math. Proc. Camb. Phil. Soc.* **46**, 603–613.

JANSSEN, R. & ARMFIELD, S. W. 1996 Stability properties of the vertical boundary layers in differentially heated cavities. *Intl J. Heat Fluid Flow* **17** (6), 547–556.

KE, J., WILLIAMSON, N., ARMFIELD, S. W., MCBAIN, G. D. & NORRIS, S. E. 2019 Stability of a temporally evolving natural convection boundary layer on an isothermal wall. *J. Fluid Mech.* **877**, 1163–1185.

KE, J., WILLIAMSON, N., ARMFIELD, S. W., NORRIS, S. & KIRKPATRICK, M. P. 2018 Direct numerical simulation of a temporally developing natural convection boundary layer on a doubly infinite isothermal wall. In *International Heat Transfer Conference Digital Library, IHTC-16*. Begel House Inc.

KIŠ, P. & HERWIG, H. 2012 The near wall physics and wall functions for turbulent natural convection. *Intl J. Heat Mass Transfer* **55** (9–10), 2625–2635.

KLEWICKI, J. C. 2010 Reynolds number dependence, scaling, and dynamics of turbulent boundary layers. *J. Fluids Engng* **132** (9), 094001.

KOZUL, M., CHUNG, D. & MONTY, J. P. 2016 Direct numerical simulation of the incompressible temporally developing turbulent boundary layer. *J. Fluid Mech.* **796**, 437–472.

MARUSIC, I. & MONTY, J. P. 2019 Attached eddy model of wall turbulence. *Annu. Rev. Fluid Mech.* **51**, 49–74.

MARUSIC, I., MONTY, J. P., HULTMARK, M. & SMITS, A. J. 2013 On the logarithmic region in wall turbulence. *J. Fluid Mech.* **716**, R3.

NAKAO, K., HATTORI, Y. & SUTO, H. 2017 Numerical investigation of a spatially developing turbulent natural convection boundary layer along a vertical heated plate. *Intl J. Heat Fluid Flow* **63**, 128–138.

NG, C. S., CHUNG, D. & OOI, A. 2013 Turbulent natural convection scaling in a vertical channel. *Intl J. Heat Fluid Flow* **44**, 554–562.

NG, C. S., OOI, A., LOHSE, D. & CHUNG, D. 2017 Changes in the boundary-layer structure at the edge of the ultimate regime in vertical natural convection. *J. Fluid Mech.* **825**, 550–572.

NICKELS, T. B. 2004 Inner scaling for wall-bounded flows subject to large pressure gradients. *J. Fluid Mech.* **521**, 217–239.

PERRY, A. E. & CHONG, M. S. 1982 On the mechanism of wall turbulence. *J. Fluid Mech.* **119**, 173–217.

POPE, S. B. 2000 *Turbulent Flows*. Cambridge University.

PRANDTL, L. 1925 Bericht über untersuchungen zur ausgebildeten turbulenz. *Z. Angew. Math. Mech.* **5** (2), 136–139.

PRANDTL, L. 1932 Zur turbulenten strömung in rohren und längs platten. *Ergebnisse der aerodynamischen versuchsanstalt zu göttingen* **4**, 18–29.

SAYADI, T., HAMMAN, C. W. & MOIN, P. 2013 Direct numerical simulation of complete h-type and k-type transitions with implications for the dynamics of turbulent boundary layers. *J. Fluid Mech.* **724**, 480–509.

SCHETZ, J. A. & EICHHORN, R. 1962 Unsteady natural convection in the vicinity of a doubly infinite vertical plate. *J. Heat Transfer* **84** (4), 334–338.

SHIRI, A. & GEORGE, W. K. 2008 Turbulent natural convection in a differentially heated vertical channel. In *ASME 2008 Heat Transfer Summer Conference Collocated with the Fluids Engineering, Energy Sustainability, and 3rd Energy Nanotechnology Conferences*, pp. 285–291. American Society of Mechanical Engineers Digital Collection.

TOWNSEND, A. A. 1951 The structure of the turbulent boundary layer. *Math. Proc. Camb. Phil. Soc.* **47**, 375–395.

TOWNSEND, A. A. 1961 Equilibrium layers and wall turbulence. *J. Fluid Mech.* **11** (1), 97–120.

TOWNSEND, A. A. 1976 *The Structure of Turbulent Shear Flow*. Cambridge University.

TSUJI, T. & NAGANO, Y. 1988 Characteristics of a turbulent natural convection boundary layer along a vertical flat plate. *Intl J. Heat Mass Transfer* **31** (8), 1723–1734.

VERSTEEGH, T. A. M. & NIEUWSTADT, F. T. M. 1999 A direct numerical simulation of natural convection between two infinite vertical differentially heated walls scaling laws and wall functions. *Intl J. Heat Mass Transfer* **42** (19), 3673–3693.

VON KÁRMÁN, T. 1930 Mechanische änlichkeit und turbulenz. *Nachrichten von der Gesellschaft der Wissenschaften zu Göttingen, Mathematisch-Physikalische Klasse* **1930**, 58–76.

WEI, T. 2019 Scaling of reynolds stresses in a differentially heated vertical channel. *Phys. Rev. Fluids* **4** (5), 051501.

WELLS, A. J. & WORSTER, M. G. 2008 A geophysical-scale model of vertical natural convection boundary layers. *J. Fluid Mech.* **609**, 111–137.

WILLIAMSON, N., ARMFIELD, S. W. & KIRKPATRICK, M. P. 2012 Transition to oscillatory flow in a differentially heated cavity with a conducting partition. *J. Fluid Mech.* **693**, 93–114.

YAGLOM, A. M. 1979 Similarity laws for constant-pressure and pressure-gradient turbulent wall flows. *Annu. Rev. Fluid Mech.* **11** (1), 505–540.

ZHAO, Y., LEI, C. & PATTERSON, J. C. 2013 Resonance of the thermal boundary layer adjacent to an isothermally heated vertical surface. *J. Fluid Mech.* **724**, 305–336.

ZHAO, Y., LEI, C. & PATTERSON, J. C. 2017 The k-type and h-type transitions of natural convection boundary layers. *J. Fluid Mech.* **824**, 352–387.